PHYSICAL REVIEW B **108**, 094110 (2023)

Pressure-induced structural transformations in $(1-x)\mathrm{Na}_{0.5}\mathrm{Bi}_{0.5}\mathrm{TiO}_3-x\mathrm{BaTiO}_3$ at the morphotropic phase boundary

Constanze Rösche ,[1,*] Tiziana Boffa-Ballaran ,[2] and Boriana Mihailova [1]
[1]*Department of Earth System Sciences, Universität Hamburg, Grindelallee 48, 20146 Hamburg, Germany*
[2]*Bayerisches Geoinstitut, Universität Bayreuth, Universitätsstraße 30, 95440 Bayreuth, Germany*

(Received 5 May 2023; revised 2 August 2023; accepted 5 September 2023; published 22 September 2023)

Pressure-induced structural transformations up to 8.9 GPa in the perovskite-type ($AB\mathrm{O}_3$) $(1-x)\mathrm{Na}_{0.5}\mathrm{Bi}_{0.5}\mathrm{TiO}_3-x\mathrm{BaTiO}_3$ (NBT-xBT) at the morphotropic phase boundary (MPB), $x_{\mathrm{MPB}} = 0.048$, were studied by means of polarized Raman spectroscopy and single-crystal x-ray diffraction. Raman spectroscopic analysis was also performed on reference undoped NBT to reveal the effect of chemical composition on the response of the atomic dynamics to isotropic elastic stress. Our results demonstrate that, like Pb-based relaxors and pure NBT, NBT-0.048BT undergoes multistep structural alteration to a high-pressure state consisting of reduced off-centered displacements of B-site cations, enhanced antipolar order of off-centered shifts of A-site cations, and induced $B\mathrm{O}_6$ tilt order. The comparison between NBT and NBT-0.048BT reveals that Ba doping at the level of the MPB composition smears out the pressure range of ongoing structural transformations, slows down the suppression of off-centering for both A- and B-site cations, and hardens the A-cation subsystem but softens the B-cation subsystem. The larger volume compressibility of NBT-0.048BT with respect to NBT suggests that the softening of the B-cation subsystem due to the substitution of Ba controls the bulk compressibility at the MBP.

DOI: 10.1103/PhysRevB.108.094110

I. INTRODUCTION

Perovskite-type ($AB\mathrm{O}_3$) ferroelectrics are widely used functional materials which have found numerous applications in electronic devices such as sensors, actuators, and capacitors [1]. Currently, mainly Pb-based perovskite-type ferroelectric materials are in industrial use, but due to continuously growing concerns related to the toxicity of lead, they should be replaced by ecologically friendly alternatives in the near future. Solid solutions exhibiting a morphotropic phase boundary (MPB), where the symmetry of the ferroelectric phase changes upon compositional variations and the material properties are enhanced, are of particular interest, as small changes in the composition affect the nanoscale structure, which in turn allows for tuning the properties [2–4]. The ferroelectric solid solution $(1-x)\mathrm{Na}_{0.5}\mathrm{Bi}_{0.5}\mathrm{TiO}_3-x\mathrm{BaTiO}_3$ (NBT-xBT) is a promising candidate as a lead-free functional material because it exhibits heavy nanoscale structural inhomogeneities [5–8] and a MPB at $x = 0.5-0.6$, where the dielectric permittivity, piezoelectric coefficient, and electromechanical coupling factor are strongly boosted [9–12]. The existence of polar nanoregions (PNRs), consisting of cationic off-center displacements with a coherence length of only a few nanometers, was suggested for NBT-xBT with $0 \leqslant x \leqslant x_{\mathrm{MPB}}$ [13,14], like the structural state of Pb-based relaxor ferroelectrics [15], while the occurrence of nanoregions comprising polar shifts of A-site cations that are antiparallel to those of the B-site cations was proposed for compositions with $x_{\mathrm{MPB}} \leqslant x \leqslant 0.11$, giving rise to the so-called relaxor antiferroelectric state [16]. Authors of further studies have indicated that, for Ba-doped NBT with $0.013 \leqslant x \leqslant 0.074$, mesoscopic-scale antiferroelectric order in the A-cation subsystem coexists with mesoscopic-scale ferroelectric order within the B-cation subsystem between the temperature of the dielectric-permittivity maximum T_m and the depoling temperature T_d [17,18]. Pure NBT is characterized by local-scale A-site chemical order [19–23] and octahedral tilting [24]. The addition of BaTiO_3 to NBT induces extra local strains in the structure [17,25], which suppress the octahedral tilts while favoring polar Ti displacements from the $B\mathrm{O}_6$ centers [17]. Furthermore, doping with BaTiO_3 reduces the average size of PNRs but increases their fraction [26,27]. At ambient conditions, with the increase of Ba content, NBT-xBT undergoes a series of composition-induced phase transitions, involving transformations of the $B\mathrm{O}_6$-tilt pattern. The end member NBT was assumed to exhibit rhombohedral symmetry ($R3c$), but meanwhile, it has been proven this is only true for poled samples [28]. The structure of unpoled NBT is in fact monoclinic (Cc) [29] with tilt pattern $a^-a^-c^-$ [8] (Glazer notation [30]). Only at $x = 0.03-0.04$ does the symmetry transform to rhombohedral $R3c$ with tilt pattern $a^-a^-a^-$ also in the absence of an electric field [31]. Near $x_{\mathrm{MPB}} = 0.05-0.06$, $a^0a^0c^+$ in-phase tilting occurs, changing the symmetry to $P4bm$, and at $x = 0.10-0.11$, the structure adopts the same $B\mathrm{O}_6$ tilt-free tetragonal $P4mm$ symmetry as BaTiO_3 [31]. The MPB is at $x \sim 0.05$ for unpoled single crystals [32,33] ($x \sim 0.06$ for unpoled ceramics [9]), and the structure becomes pseudocubic [34]. At this composition, NBT-xBT shows an enhanced flexibility of the local dipoles, which may be caused

---

[*] constanze.roesche@uni-hamburg.de

by increasing decoupling of strain and polarization as well as reduced competing local correlations, leading to reduced local strains [23,35]. Moreover, an increased self-organization between PNRs along the ⟨110⟩ direction has been observed by means of piezoresponse force microscopy, polarized light microscopy, and transmission electron microscopy (TEM) for compositions approaching the MPB [26,27], which is consistent with the shape and abnormally large correlation length of the neutron diffuse scattering observed for NBT-0.05BT [36].

Despite the similarities between NBT-*x*BT and Pb-based ferroelectric perovskites, the properties of NBT-*x*BT are somehow inferior [37]. Chemical variations can tune the local ferroic atomic clustering [38]; therefore, the properties could be improved by additional *A*- or *B*-site doping [39]. Knowledge of the relation between chemical composition and structural features is key for efficiently designing high-performance functional materials, and thus, deeper understanding of the complex nanoscale structure of NBT-*x*BT is required. This can be reached by studying the response of the structure to external stimuli such as temperature, elastic stress, or electric field at different length scales. Several studies in which authors examined the effect of temperature and electric field have been conducted [17,18,35], but high-pressure studies on NBT-*x*BT are still scarce, although essential, since the application of pressure can help revealing subtle structural features, which are hard to detect at ambient pressure [40,41].

Authors of previous high-pressure studies combining x-ray diffraction (XRD) and Raman scattering, i.e., probing long-range and short-rang order, respectively, have revealed that Pb^{2+}-based $AB\mathrm{O}_3$-type relaxor ferroelectrics undergo two pressure-induced phase transitions in the range up to ∼25 GPa, whose critical pressures p_{c1} and p_{c2} strongly depend on the chemical composition, and each phase transition is preceded by local-scale structural transformations at characteristic pressures $p_1^* < p_{c1}$ and $p_2^* < p_{c2}$ [41–43]. The first phase transition at p_{c1} consists of a change from relaxor cubic to a rhombohedral nonpolar state with long-range order of antiphase octahedral tilts, which is preceded by the suppression of dynamical coupling between off-centered *A*- and *B*-site cations at p_1^*. At the second phase-transition pressure p_{c2}, long-range order of antipolar *A*-cation displacements together with $a^-a^-c^+$ octahedral tilts is developed, or a sole long-range order of $a^-a^-c^-$ tilt ($0 \leqslant c < a$) order occurs. This second transition is preceded by the formation of unequal octahedral tilts on the local scale at p_2^* [41,42]. From these observations, it could be deduced that, at ambient conditions, ferroelectric and antiferrodistortive order coexist on the mesoscopic scale in $AB\mathrm{O}_3$-type relaxors, indicating that the nature of the PNRs is ferrielectric [41,42,44–46]. Since the structure of NBT-*x*BT near MBP is rather like that of perovskite-type Pb^{2+}-based relaxors [47], high-pressure structural analyses are needed to shed further light onto the nanoscale structural inhomogeneities of Pb-free ferroelectric solid solutions.

So far, only the high-pressure behavior of pure NBT has been extensively studied by various analytical methods including powder synchrotron XRD and neutron diffraction [48,49], single-crystal XRD [19,48] and x-ray diffuse scattering [19], powder Raman spectroscopy [50], and differential thermal analysis [51]. The results obtained from the methods sensitive to long-range order suggest that multiple structural transformations take place from 0.7 to 4 GPa, which are mostly interpreted as phase transition from rhombohedral *R3c* to orthorhombic *Pnma* symmetry through a state of phase coexistence [48,49]. This assumption is supported by *ab initio* calculations [21]. Single-crystal synchrotron XRD analysis revealed a transition at 1.6–2.0 GPa to a lower-symmetry phase, followed by gradual structural changes on the short-range scale between 2.8 and 3.7 GPa, where the ferroic distortions in PNRs are synchronized with those in the matrix [19]. Furthermore, the data imply a second phase transition between 9.9 and 11.1 GPa to a noncubic phase [19], whose true symmetry has not been determined [49]. Powder Raman spectroscopic data, on the other hand, indicate that structural transformations proceed from 2.7 to 5 GPa [50]. The available high-pressure data of NBT-*x*BT are limited to Raman spectroscopic studies on NBT [50] and NBT-0.11BT powders [52] as well as on NBT-0.065BT single crystals [53], neither of which, however, consider the important spectral range $<80\,\mathrm{cm}^{-1}$, dominated by atomic vibrations of off - centered *A*-site cations [54]. Moreover, the use of powder, as in the case of NBT and NBT-0.11BT, or nonhydrostatic pressure-transmitting media, as in the case of NBT-0.065BT, may give rise to undesired nonhydrostatic stresses during the high-pressure experiments, which undermines the quantitative analysis of intrinsic material properties [55,56]. Nevertheless, it has been shown that NBT-*x*BT ferroelectrics with $x = 0.065$ and 0.11 undergo similar pressure-induced transformations as undoped NBT, but the presence of Ba shifts the structural alterations to higher pressures [52]. No data exist for compositions close to the MPB though.

Here, we report on the results of high-pressure Raman spectroscopy of single crystals of NBT-*x*BT at the MPB ($x = 0.048$ [17]) and pure NBT in the entire spectral range of fundamental phonons ($15{-}1215\,\mathrm{cm}^{-1}$) up to 10 GPa as well as high-precision single-crystal XRD data on NBT-0.048BT up to 6.1 GPa. All measurements have been conducted under hydrostatic conditions using a methanol : ethanol or methanol : ethanol : water pressure-transmitting medium. The goal of our study was to analyze the composition-related difference between the pressure-induced structural transformations in NBT-*x*BT for $x = x_{\mathrm{MPB}}$ and $x = 0$ to give further insight into the MPB structure.

II. EXPERIMENTAL DETAILS

A. Samples

Single crystals of (1–*x*)NBT-*x*BT with $x = 0$ and 0.048 were synthesized by the top-seeded-solution-growth method [57]. The chemical composition was verified by wavelength-dispersive x-ray emission spectroscopy, and the unit-cell parameters at ambient conditions were determined by single-crystal XRD [17]. Both single-crystal compounds are chemically homogeneous and appear pseudocubic under in-house XRD examination. At room temperature and atmospheric pressure, the unit-cell parameters best match rhombohedral metrics, with $a = b = c = 3.884\,\text{Å}$ and $90^\circ - \alpha_{\mathrm{rh}} = 0.045^\circ$ for $x = 0$, and $a = b = c = 3.896\,\text{Å}$ and $90^\circ - \alpha_{\mathrm{rh}} = 0.015^\circ$ for $x = 0.048$ [17]. For the high-pressure experiments,

~40-μm-thick specimens cut parallel to one of the pseudocubic {100} planes were prepared using a diamond wire.

B. High-pressure Raman spectroscopy

In situ high-pressure Raman-scattering experiments were conducted in a Boehler-Almax diamond anvil cell (DAC) [58] with a culet diameter of 600 μm. The sample chamber was prepared by preindenting a stainless-steel gasket to ~92 μm and drilling a 300 μm hole with a Boehler microDriller spark erosion device. Hydrostatic conditions up to 10.5 GPa were ensured by using a 16:3:1 methanol : ethanol : water mixture as a pressure transmitting medium [55]. The pressure in the sample chamber was determined with an uncertainty of ~0.05 GPa using the ruby-line photoluminescence method [59].

The Raman spectra were measured with a Horiba Jobin-Yvon T64000 triple-grating spectrometer equipped with an Olympus BH41 microscope and a 50× long-working-distance objective, using the 514.5 nm line of a Coherent Innova 90C FreD Ar^+ laser. The spectrometer operated in a subtractive regime to ensure maximum suppression of the Rayleigh scattering without artificially distorting the Raman signal [60]. The spectral resolution was $\sim 2\,\mathrm{cm}^{-1}$, and the accuracy of the peak position was $0.35\,\mathrm{cm}^{-1}$. Parallel polarized ($\mathbf{E}_i || \mathbf{E}_s$, where $\mathbf{E}_i$ and $\mathbf{E}_s$ represent the polarization of the incident and scattered light) and cross-polarized ($\mathbf{E}_i \perp \mathbf{E}_s$) Raman spectra in the range $15-1215\,\mathrm{cm}^{-1}$ were collected in backscattering geometry, resulting in the scattering geometries $\bar{Z}(XX)Z$ and $\bar{Z}(XY)Z$ (Porto's notation) with X, Y, and Z parallel to the three pseudocubic ⟨100⟩ directions. Reproducibility of the spectra was proven by collecting data from at least two different spatial points at every pressure.

For NBT-0.048BT, two different pressure runs were conducted with the same specimen: up to 4.5 and 8.9 GPa. Note that the orientation of the sample during the first run was slightly different (rotated by ~10°) from that during the second run. This was due to the subtle depolarizing effect of diamond anvils, which hindered finding the crystal orientation, yielding the strongest difference between $\bar{Z}(XX)Z$ and $\bar{Z}(XY)Z$ spectra. For pure NBT, a single pressure run was conducted up to 10.6 GPa. In all experiments, the pressure was increased in small steps (~0.2−0.3 GPa), and after each pressure change, the sample was given time to relax before data acquisition. Additional spectra were recorded on decompression after reaching the highest pressure to verify reversibility of the pressure-induced changes. Furthermore, at each pressure, the Raman signal of the diamond anvils was measured in the range $1050-1610\,\mathrm{cm}^{-1}$ to track the changes in diamond optical properties due to the stress-induced morphic effect, which leads to an increasing degree of depolarization of the Raman spectra [61].

To remove the contribution from the diamond anvils and the pressure transmitting medium to the Raman spectrum of the sample, a background spectrum was collected from an area next to the crystal using the same experimental conditions, normalized to the height of the Raman peaks generated by the pressure medium that could be resolved in the spectrum collected from the sample, and subsequently subtracted. The Raman intensities of the background-corrected spectra were temperature reduced by the Bose-Einstein phonon occupation factor and then fitted with pseudo-Voigt functions to determine the phonon wave numbers (ω), full widths at half maximum (FWHMs, Γ), and integrated intensities (I). The data evaluation was performed with the OriginPro 2021 software package [62].

C. High-pressure single-crystal XRD

Two sets of high-pressure XRD experiments were performed up to 6.1 and 1.6 GPa using two different specimens of ~60 × 60 × 40 μm dimensions from the same bulk crystal. The purpose of the second experiment was to collect additional points in the low-pressure range and confirm the reproducibility of the data. In the first run, a BX90 DAC [63] with 500 μm culets was used, while the second run was conducted using a Boehler-Almax DAC [58] with 600 μm culets. Stainless steel gaskets were preindented to 70 and 96 μm, respectively, and 280 μm holes were generated by laser drilling. The pressure transmitting medium was a 16:3:1 methanol : ethanol : water mixture in the first and a 4:1 methanol : ethanol mixture in the second experiment, which are hydrostatic up to 10.5 and 9.8 GPa, respectively [55,64]. In the first run, the fluorescence spectra of ruby measured before and after the x-ray measurements were used for determining pressure [59], whereas in the second run, the unit-cell volume of quartz [65] loaded together with the NBT-0.048BT crystal was used instead, allowing us to determine the pressure with accuracy <0.01 GPa.

High-pressure single-crystal XRD was performed using a four circle Huber Eulerian goniometer coupled with an ultrahigh-intensity rotating anode x-ray source with Mo $K\alpha$ radiation equipped with a multilayer VaryMax focusing optic and a point detector [66]. The rotating anode was operated at 45 kV and 55 mA, and the diffractometer was driven by SINGLE software [67]. Unit-cell lattice parameters were determined by the vector least-squares method [68], using up to 12 unique reflections centered in eight positions [69] to eliminate the effect of crystal offsets and diffractometer aberrations. Because of the specific orientation of the single-crystal cuts, being parallel to one of the pseudocubic {100} crystallographic planes, only two of the three unconstrained unit-cell lattice parameters could be determined with high accuracy and precision at all pressure points with uncertainties <0.0002 Å. The uncertainties on the third unit-cell parameter were instead >0.001 Å.

III. RESULTS AND DISCUSSION

A. Raman spectroscopy

1. Spectra at ambient conditions: Symmetry considerations and peak assignment

The Raman spectra of NBT and NBT-0.048BT measured at ambient conditions are shown in Fig. 1. A detailed group-theory analysis for NBT-xBT is given by Datta *et al.* [70]. For NBT-xBT with monoclinic (Cc), rhombohedral ($R3c$), or tetragonal ($P4bm$) symmetry 27, 13, and 16 Raman active modes are predicted, respectively. If longitudinal optical (LO)-transverse optical (TO) effects for polar Raman active modes are considered, the number of observable Raman peaks

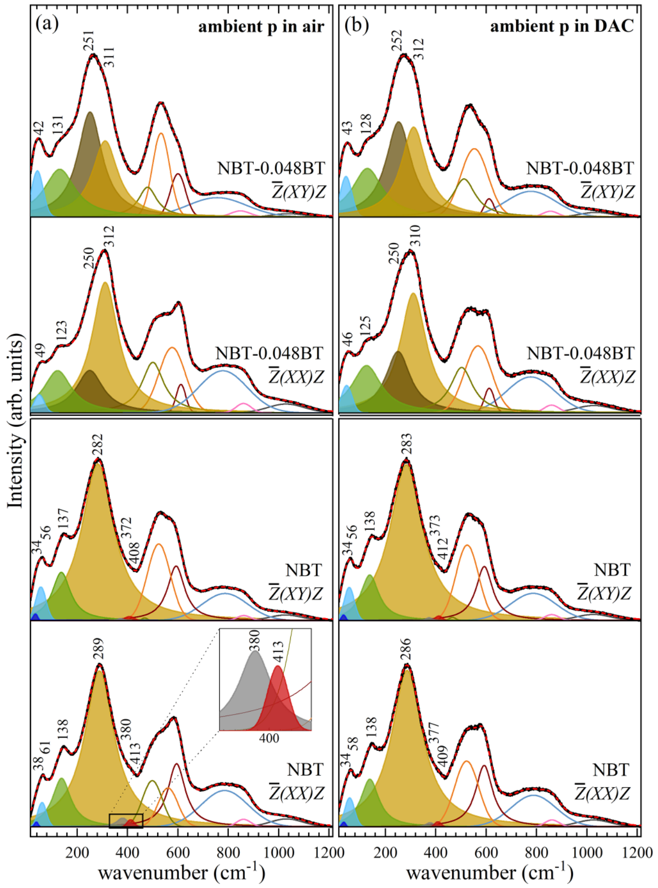

FIG. 1. Polarized $\bar{Z}(XX)Z$ and $\bar{Z}(XY)Z$ Raman spectra (solid black lines) of NBT-0.048BT and NBT measured (a) at ambient conditions in air and (b) inside the diamond anvil cell without pressure transmitting medium, along with the fitting pseudo-Voigt functions and the resultant spectrum profiles (red dashed lines). The insert in (a) shows the tilt modes in an enlarged scale.

is 54 (Cc), 26 ($R3c$), or 28 ($P4bm$). However, a considerably smaller number of peaks could be resolved for both pure NBT and NBT-0.048BT. Thus, the spectra were fitted using the model presented by de la Flor *et al.* [17], which was developed analyzing samples from the same synthesis batch as in this study at different temperatures as well as under an external electric field [17,18,35]. Peaks were added or removed in the high-pressure spectra following the standard goodness-of-fit criteria, including $\Delta I/I < 0.5$ for all peaks, where ΔI is the absolute error in the integrated intensity I [17,70]. The fitting procedure is described in detail in the Supplemental Material, Text SI [71].

The Raman scattering at 30–60 and $240-310\,\mathrm{cm}^{-1}$ is associated with the A- and B-site cation shifts from the centers of the AO_{12} dodecahedra and BO_6 octahedra, respectively [54,70,72]. The range $120-160\,\mathrm{cm}^{-1}$ is dominated by the $A-BO_3$ translation modes, which are sensitive to the coupling between the dipoles at adjacent A and B sites [70,73]. The Raman scattering arising from A-cation vibrations is most likely dominated by Bi vibrations due to the more covalent character of the Bi-O bonds as compared with the Na-O and Ba-O bonds as well as the large off-centered displacement of Bi^{3+} [70,74] related to its affinity to form stereochemically active electronic lone pairs in 12th coordination [54]. The TiO_6 octahedral tilting modes, which can be considered also as A-O bond stretching vibrations within pseudocubic $\langle 111\rangle$ planes, are located at $\sim 320-420\,\mathrm{cm}^{-1}$ [17,75,76]. The Raman peaks in the range $470-820\,\mathrm{cm}^{-1}$ arise from internal BO_6 vibrations [54,75,76]. Due to the larger partition of oxygen vibrations, these peaks are broader than the peaks $<470\,\mathrm{cm}^{-1}$, and consequently, the peak overlapping is stronger, which results in larger dispersions of the fitted wave numbers, FWHMs, and relative intensities. Hence, we will not consider in detail the pressure evolution of BO_6-internal modes.

The substitution of Ba into the NBT structure in the sample with $x = 0.048$ slightly changes the Raman spectrum [see Fig. 1(a)]. Within the range $30-60\,\mathrm{cm}^{-1}$, only one peak (light blue), instead of two (see Supplemental Material Text SI [71]), can be distinguished for the NBT-0.048BT, which most probably results from the increased disorder within the subsystem of A-site dipoles due to Ba doping. The peak associated with the $A-BO_3$ translation mode [in green, Fig. 1(a)], which appears in the range $120-160\,\mathrm{cm}^{-1}$, exhibits a lower wave number and larger FWHM than pure NBT due to composition-induced softening of this mode caused by the increased coupling between the adjacent off-centered A- and B-site cations at the MPB [23,70]. Furthermore, two Raman peaks related to off-centered B-site cations (brown and yellow, in the range $240-310\,\mathrm{cm}^{-1}$) can be resolved for NBT-0.048BT, whereas only one peak is visible for NBT, indicating the presence of a uniaxial local anisotropy of the BO_6 octahedra. The higher wave number component is associated with B-cation vibrations along the polar axis, whereas the lower wave number component represents B-cation vibrations within the perpendicular planes [35]. The sole broad peak observed for NBT in both scattering geometries [Fig. 1(a) bottom] most probably results from overlapping of the multiple B-cation-related Raman peaks expected in monoclinic perovskite-type oxides [77], contributing with similar weights to $\bar{Z}(XX)Z$ and $\bar{Z}(XY)Z$ polarized spectra. The BO_6 tilting modes in the range $370-420\,\mathrm{cm}^{-1}$ appear only with a very weak intensity in pure NBT [see the insert in Fig. 1(a)] and are not observed at all in NBT-0.048BT.

The comparison of the polarized Raman spectra of the NBT and NBT-0.048BT samples obtained inside [Fig. 1(b)] and outside [Fig. 1(a)] of a DAC shows that the optical properties of the diamond anvils interfere with the polarization of the incident and scattering light, reducing the difference between the $\bar{Z}(XX)Z$ and $\bar{Z}(XY)Z$ spectra already at ambient conditions. As pressure increases, the depolarizing effect of the stressed diamonds also increases [61]. However, a clear distinction between the two scattering geometries was still maintained at the highest pressure measured.

2. *Spectra at high pressures*

In general, the Raman spectra of NBT-0.048BT and pure NBT (Fig. 2) show a pressure evolution like that of Pb-based perovskite-type ferroelectrics [40,43,45,46,78]. First, the intensity of the phonon modes associated with off-centering of the B-site cations ($\sim 240-310\,\mathrm{cm}^{-1}$) is strongly reduced. Simultaneously, the intensity in the spectral region from 300 to $400\,\mathrm{cm}^{-1}$, where octahedral tilting modes are observed, is

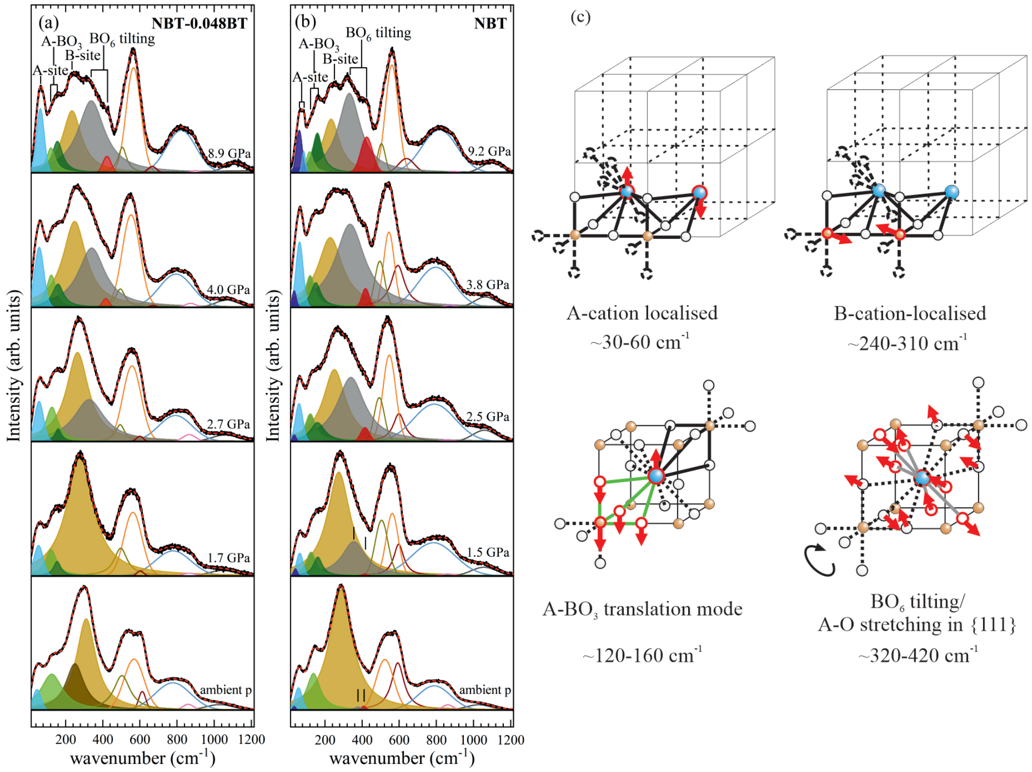

FIG. 2. Selected polarized $\bar{Z}(XX)Z$ Raman spectra of (a) NBT-0.048BT and (b) NBT measured at different pressures (solid black line), along with the fitting pseudo-Voigt functions and the resultant spectrum profiles (red dashed lines). For each compound, a comprehensive set of spectra measured at approximately every 0.5 GPa is given in Fig. S2 in the Supplemental Material [71]. Sketches of atomic vibrations for the modes generating the shaded peaks are given in (c) (after Refs. [17,40,75]).

enhanced. In other words, pressure suppresses the polar order, while it promotes the antiferrodistortive order in NBT-xBT, as in the case of Pb-based ferroelectrics [40]. These structural changes are fully reversible on decompression. Qualitatively, our results are in good agreement with previous studies of NBT [50] and NBT-0.11BT [52].

Below, we analyze in detail the pressure dependencies of the wave numbers ω (values are listed in Tables SI–SIII in the Supplemental Material [71]), FWHMs or Γ, and fractional intensities $I_n(s) = I(s)/\sum_s I(s)$ of the Raman peaks in the range $15-450\,\mathrm{cm}^{-1}$. The trends of NBT-0.048BT derived from the spectra measured in different scattering geometries reveal the same pressure evolution; therefore, only the $\bar{Z}(XX)Z$ data are shown. In contrast, for pure NBT, the pressure evolutions of the peaks corresponding to the same type of vibration measured with $\mathbf{E}_i \,||\, \mathbf{E}_s$ or $\mathbf{E}_i \perp \mathbf{E}_s$ significantly deviate from each other. This difference mirrors the lower symmetry of the average structure of undoped NBT as compared with the pseudocubic NBT-0.048BT at MPB [17,34].

(a) A-cation localized mode. The pressure evolutions of ω, Γ, and I_n of the A-cation localized modes near $30-60\,\mathrm{cm}^{-1}$ are shown in Fig. 3. As mentioned above, only one peak related to the A-cation vibrations is distinguished for NBT-0.048BT at $\sim 46\,\mathrm{cm}^{-1}$, while for pure NBT, two components can be resolved at ~ 34 and $\sim 58\,\mathrm{cm}^{-1}$ in the parallel polarized spectra and at ~ 34 and $\sim 56\,\mathrm{cm}^{-1}$ in the cross-polarized spectra. Thus, to compare the trends for both compounds, the square root of the average square wave number $\omega_{34,58} = \sqrt{(\omega_{34}^2 + \omega_{58}^2)/2}$, an effective FWHM $\Gamma_{34,58} = (\omega_{58} - \omega_{34}) + \frac{\Gamma_{34}+\Gamma_{58}}{2}$ (see also the sketch in Fig. S3 in the Supplemental Material [71]), and the sum of the fractional intensities $I_{n34,58} = I_{n34} + I_{n58}$ of the two peaks in NBT were considered as a function of pressure and compared with the corresponding trends for NBT-0.048BT (see Fig. 3). The pressure dependences of the two individual components at ω_{34} and ω_{58} for NBT are given in Fig. S4 in the Supplemental Material [71].

For NBT-0.048BT, the wave number of the A-cation mode [Fig. 3(a)] gradually increases with pressure up to 1.9 ± 0.1 GPa and above $\sim 4.3 \pm 0.6$ GPa, with a plateaulike feature in between, which indicates ongoing structural transformations driven by rearrangements within the A-site sublattice. To better reveal the trends of the FWHM and fractional intensity, the variations with pressure of $\Gamma(p)$ and $I_n(p)$ were fitted with Gaussian functions using polynomial baselines to account for the anharmonic background [79]. The start and endpoint of the wave number plateau are accompanied by maxima in the FWHM at 1.5 ± 0.1 and 4.8 ± 0.2 GPa, whereas the fractional intensity considerably increases and exhibits a maximum at 4.9 ± 0.2 GPa. In general, pressure does not change the phonon decay, and therefore, $\Gamma(p)$ should remain constant as a function of pressure. Hence, following the concept of hard-mode spectroscopy [79], the excess FWHM as well as the nonlinear behavior of the fractional intensity (Fig. 3) confirm the pressure range of ongoing structural transformations indicated by $\omega(p)$. The overall increase in intensity, as

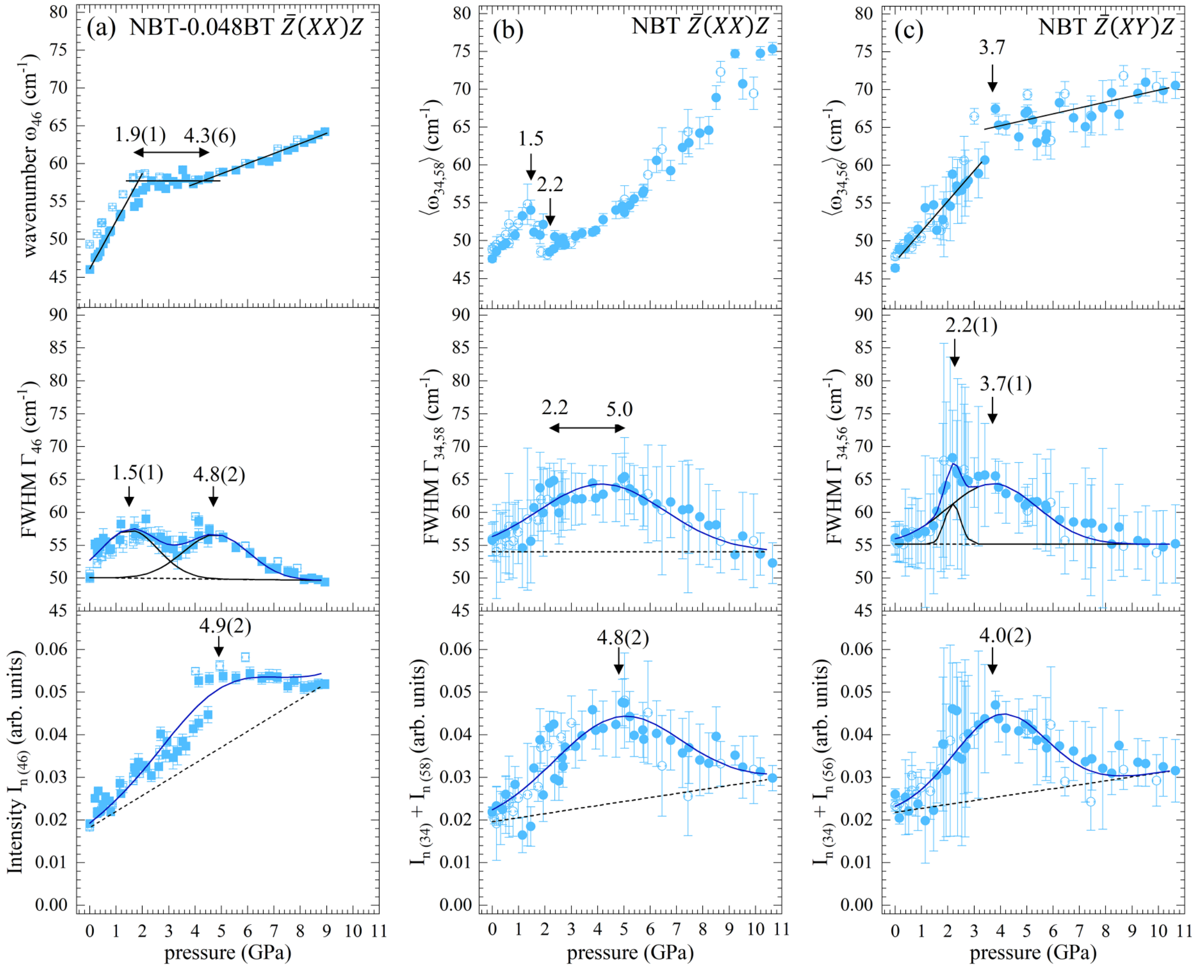

FIG. 3. Pressure dependence of the Raman peak positions (ω), full widths at half maxima (FWHMs; Γ), and fractional intensities (I_n) of the *A*-cation localized mode in parallel polarized spectra of (a) NBT-0.048BT and (b) NBT as well as (c) in cross-polarized spectra of NBT. For NBT-0.048BT, the trends in the cross-polarized spectra are the same as in the parallel polarized spectra shown here. For better comparability, the average square wave number $\langle\omega_{1,2}\rangle = \sqrt{(\omega_1^2 + \omega_2^2)/2}$, an effective FWHM $\Gamma_{1,2} = (\omega_2 - \omega_1) + \frac{\Gamma_1+\Gamma_2}{2}$, and the sum of the fractional intensities of the two peaks in NBT positioned at $\omega_1 \sim 34\,\mathrm{cm}^{-1}$ and $\omega_2 \sim 58\,\mathrm{cm}^{-1}$ were considered. Open symbols correspond to data measured on decompression. Lines in the $\omega(p)$ plots in (a) and (c) are linear fits to the data points in the corresponding pressure ranges. The solid lines in the $\Gamma(p)$ and $I_n(p)$ plots are Gaussian fits to the data points with polynomial baselines (dashed lines). The errors in the individual data points stem from the corresponding spectral fit. The errors in the characteristic pressures are derived from the Gaussian fits or from the intersection points of the linear fits. The offset between ω_{46} in NBT-0.048BT measured upon compression and decompression <2.3 GPa results from the slightly different orientation of the crystal as described in Sec. II B.

demonstrated by the slope of the $I_n(p)$ baseline, indicates that the fraction of off-centered *A* cations increases with increasing pressure.

For pure NBT, $\omega_{34,58}(p)$ derived from parallel polarized spectra anomalously softens in the pressure range 1.5–2.2 GPa [Fig. 3(b)]. This softening confirms that there is a progressing phase transition to a lower-symmetry phase as suggested by synchrotron XRD [19], which starts at 1.6 GPa and is complete at ~2.0 GPa, resulting in a long-range order of antiphase *A*-site cationic displacements and mixed BO_6 tiling [19,49]. The $\omega_{34,56}(p)$ derived from the cross-polarized Raman spectra of pure NBT shows a change in $d\omega/dp$ at 3.7 ± 0.7 GPa [Fig. 3(c)], indicating a reduction of the phonon compressibility (defined as $\beta_\omega = \frac{1}{\omega_0}\frac{d\omega}{dp}$ [80]) and hence the *A*-site-cation subsystem becoming stiffer, i.e., more resistant to a pressure increase. Since such a kink is not observed for $\omega_{34,58}(p)$ derived from parallel polarized spectra, the phenomenon at ~3.7 GPa cannot be related to an overall reduction of the volume compressibility. However, this characteristic pressure perfectly matches the disappearance of the asymmetric x-ray diffuse scattering [19] due to PNRs with polar atomic displacements deviating from those in the matrix. Hence, the presence of a kink in $\omega_{34,56}(p)$ from cross-polarized Raman data can be interpreted as an improvement of the local orientation order of *A*-cation off-center shifts at 3.7 GPa. This assumption is supported by the continuously decreasing FWHM above 3.7 and 5 GPa. Despite the large uncertainties in FWHMs due to peak overlapping, two distinct maxima can be identified at 2.2 ± 0.1 and 3.7 ± 0.1 GPa for $\Gamma(p)$ derived from the cross-polarized spectra from NBT [Fig. 3(c)] and in the parallel polarized spectra $\Gamma_{34,58}(p)$ exhibits a broad plateaulike maximum between 2.2 and 5.0 GPa [Fig. 3(b)]. Thus, the $\Gamma(p)$ trends confirm the occurrence of structural transformations in NBT at ~2.2 and ~3.7 GPa but further-

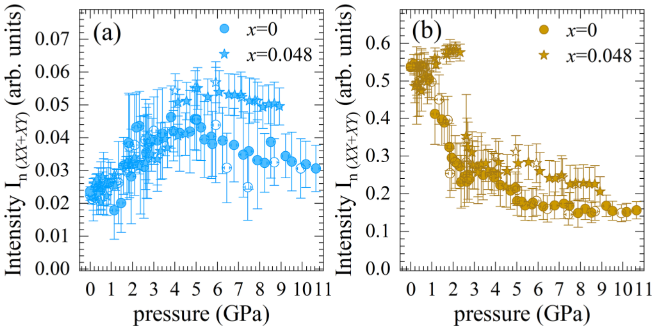

FIG. 4. Pressure dependence of the total fractional intensity $I_{n(XX+XY)}$ of the (a) A-cation and (b) B-cation localized modes in pure NBT (circles) and NBT-0.048BT (stars). $I_{n(XX+XY)}(s) = [I_{XX}(s) + I_{XY}(s)]/\Sigma_i[I_{XX}(s) + I_{XY}(s)]$, where $I_{XX}(s)$ and $I_{XY}(s)$ are the integrated intensities obtained from the Raman spectra measured in $\bar{Z}(XX)Z$ and $\bar{Z}(XY)Z$ scattering geometry for a phonon mode s. Open symbols correspond to data measured on decompression. The errors in the individual data points stem from the corresponding spectral fit.

more suggest that there are ongoing structural changes at least up to 5.0 GPa.

The comparison between the $\omega(p)$, $\Gamma(p)$, and $I_n(p)$ of pure NBT and NBT-0.048BT suggests that the latter also develops antiphase A-site cationic displacements between 1.9 ± 0.1 and 4.3 ± 0.6 GPa, the mutual alignment of which increases above 4.8 ± 0.2 GPa. However, the presence of a wave number plateau in the Ba-doped compound ($\sim$1.9−4.3 GPa) compared with the softening in pure NBT (1.5–2.2 GPa) indicates that Ba doping hinders pressure-induced structural alterations and smears out the structural changes over a broader pressure range. This effect has also been observed for Ba-doped $\mathrm{PbSc_{0.5}Ta_{0.5}O_3}$ and is assumed to be caused by Ba-induced local strains [25]. The increase in the baseline of $I_n(p)$ is much steeper in NBT-0.048BT than in pure NBT (Fig. 3), indicating a stronger pressure-induced increase in the fraction of off-centered A cations. This is supported by the total fractional intensity $I_{n(XX+XY)}(s) = [I_{XX}(s) + I_{XY}(s)]/\Sigma_s[I_{XX}(s) + I_{XY}(s)]$, where $I_{XX}(s)$ and $I_{XY}(s)$ are the integrated intensities obtained from the Raman spectra measured in $\bar{Z}(XX)Z$ and $\bar{Z}(XY)Z$ scattering geometry for a phonon mode s. For the A-site localized modes, $I_{n(XX+XY)}$ has approximately the same value in both compounds up to $\sim$4 GPa, but above 4 GPa, it is higher in the Ba-doped composition [Fig. 4(a)]. This indicates that the presence of $\mathrm{Ba^{2+}}$ cations facilitates the A-site $\mathrm{Bi^{3+}}$ off-centering upon elastic stress, thus causing a higher fraction of off-centered A-site cations in the NBT-0.048BT sample with respect to the end member.

(b) A-BO$_3$ *translation mode.* The A-$B\mathrm{O}_3$ translation mode ($120 - 160\,\mathrm{cm^{-1}}$) involves out-of-phase A-cation and $B\mathrm{O}_3$ vibrations [see Fig. 2(c)] and is sensitive to the coupling between adjacent A- and B-site dipole subsystems [23,76]. In Pb-based perovskite-type relaxors, this mode splits at a pressure ranging from 0.1 to 2.5 GPa (depending on the chemistry), preceding the phase transition due to decoupling between dipoles at adjacent A and B sites, thus allowing for suppression of B-cation off-centering and antipolar ordering of the A-site cations at higher pressures [73,78]. A splitting of the A-$B\mathrm{O}_3$ translation mode is observed at $\sim$1.2 GPa for NBT-0.048BT and at 0.3 ± 0.1 GPa for NBT (see Fig. S5 in the Supplemental Material [71] and Fig. 5), indicating the occurrence of a decoupling between dipoles at adjacent A and B sites, allowing for suppression of B-cation off-centering and antipolar ordering of the A-site cations at higher pressures. This decoupling occurs at higher pressure for NTB-0.048BT than for pure NBT, which is consistent with the proposed strengthened coupling between the dipoles at adjacent A and B sites at MPB [23]. High-pressure differential thermal analysis of pure NBT [51] has revealed that, at pressures below $\sim$0.7 GPa, NBT may undergo two temperature-induced phase transitions, like those occurring at ambient pressure, whereas at pressures above $\sim$0.7 GPa, no phase transitions are observed upon temperature increase. Our results imply that the reason for the suppression of temperature-induced phase transitions is the reduced coupling of the subsystems of off-centered A- and B-site cations.

In NBT-0.048BT, the onset of the structural transformations at 1.9 ± 0.1 GPa does not affect $\omega(p)$ of the A-$B\mathrm{O}_3$ mode, but >4.0 GPa, the slope of $\omega_{151}(p)$ changes from trivially positive to anomalously negative [see Fig. 5(a)], indicating a further change in the dynamical coupling between adjacent A- and B-site dipoles due to the ordering processes within the A-site subsystem revealed by the phonon mode at $\sim 46\,\mathrm{cm^{-1}}$ [see Fig. 3(a)]. In pure NBT, at $\sim$1.6 GPa, both $d\omega_{138}(p)/dp$ and $d\omega_{150}(p)/dp$ derived from the cross-polarized spectra become approximately zero [see Fig. 5(c)], indicating a reduction of the respective phonon compressibilities as the structure starts undergoing a phase transition. In the parallel polarized spectra, $\omega_{138}(p)$ is almost constant, while $\omega_{150}(p)$ softens from 1.6 to $\sim$4.5−5 GPa, thus reflecting the beginning of A-cation arrangements and completion of B-cation rearrangements (see the following discussion).

(c) B-cation localized mode. In the range $240{-}310\,\mathrm{cm^{-1}}$, both modes associated with off-centered B-site $\mathrm{Ti^{4+}}$ in NBT-0.048BT soften upon pressure increase [Fig. 6(a)], but they exhibit different behavior in terms of $\Gamma(p)$ and $I_n(p)$. The lower-energy component ω_{250} decreases in both intensity and FWHM. Moreover, at $\sim$0.5 GPa, $\omega_{250}(p)$ reaches a minimum and then remains constant until it cannot be distinguished anymore above $\sim$1 GPa. These trends reveal subtle structural transformations in the B-site dipole system already between 0.5 and 1.0 GPa. The higher-energy component ω_{310} also considerably softens but without an apparent minimum. However, $|d\omega_{310}(p)/dp|$ decreases above 1.2 GPa and then even further at $\sim$4.5 GPa. Interestingly, $\Gamma_{310}(p)$ and $I_{n(310)}(p)$ exhibit a maximum at $\sim$1.7 GPa. This might be partially related to an evolving $B\mathrm{O}_6$ tilting mode (see next subsection), which at low pressures cannot be energetically resolved from the B-cation mode at $\sim 310\,\mathrm{cm^{-1}}$. However, the corresponding baseline within the entire pressure range (10^{-4} to 9 GPa) clearly shows that $I_{n(310)}$ decreases, while Γ_{310} remains constant. The former further indicates that pressure suppresses the off-centering of the B-site cations, while the latter suggests that no ordering process in the B-cation subsystem takes place.

For pure NBT, the B-cation localized mode shows considerable softening up to 5 GPa [Figs. 6(b) and 6(c)], with an abrupt drop of $\omega(p)$ at 1.6 GPa in both parallel and cross-polarized spectra. The FWHM in the $\bar{Z}(XX)Z$ spectra

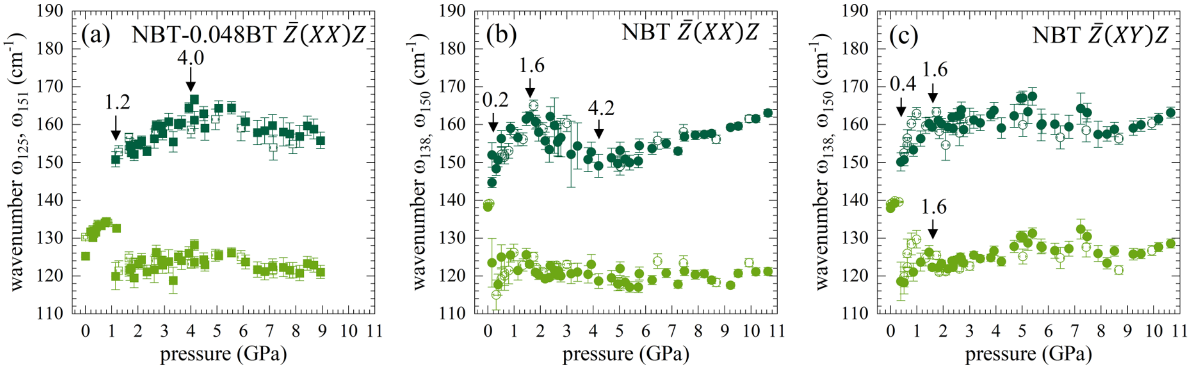

FIG. 5. Pressure dependence of the Raman peak positions (ω) of the A-BO$_3$ translation mode in parallel polarized spectra of (a) NBT-0.048BT and (b) NBT as well as (c) in cross-polarized spectra of NBT. For NBT-0.048BT, the trends in the cross-polarized spectra are the same as in the parallel polarized spectra shown here. Open symbols correspond to data measured on decompression. The errors in the individual data points stem from the corresponding spectral fit.

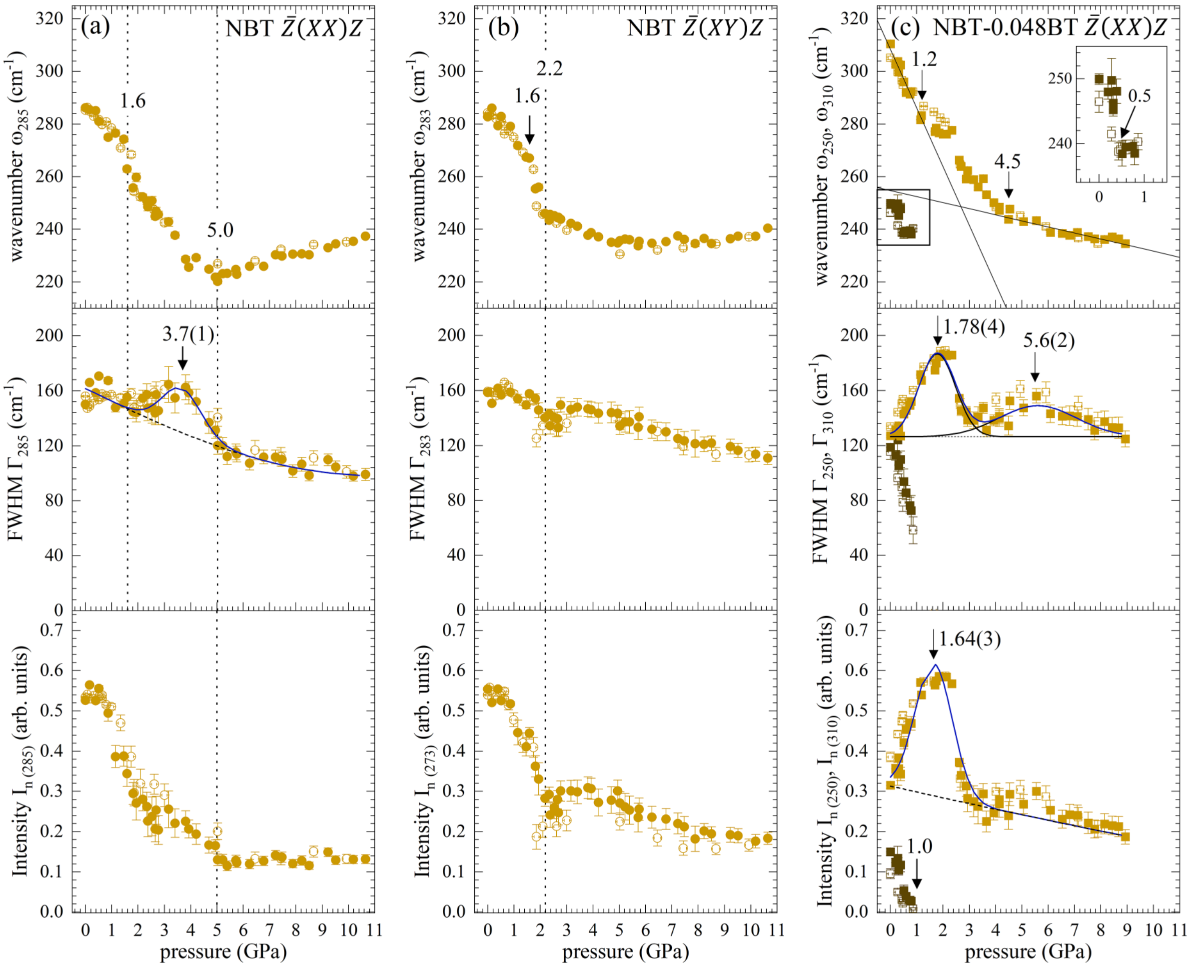

FIG. 6. Pressure dependence of the Raman peak positions (ω), full widths at half maxima (FWHMs; Γ), and fractional intensities (I_n) of the B-cation localized mode in parallel polarized spectra of (a) NBT-0.048BT and (b) NBT as well as (c) in cross-polarized spectra of NBT. For NBT-0.048BT, the trends in the cross-polarized spectra are the same as in the parallel polarized spectra shown here. Open symbols correspond to data measured on decompression. Lines in the $\omega(p)$ plot in (a) are linear fits to the data points in the corresponding pressure ranges. The solid lines in the $\Gamma(p)$ and $I_n(p)$ plots in (a) and (b) are Gaussian fits to the data points with polynomial baselines (dashed lines). The errors in the individual data points stem from the corresponding spectral fit. The errors in the characteristic pressures are derived from Gaussian or linear fits to the data points.

shows an excess between 1.6 and 5.0 GPa, with a maximum of $\Gamma(p)$ at 3.7 ± 0.1 GPa, but overall, $\Gamma(p)$ in both $\bar{Z}(XX)Z$ and $\bar{Z}(XY)Z$ anomalously decreases with pressure. At the same time, the Raman intensity of the B-localized modes strongly decreases up to 2.2 GPa in the $\bar{Z}(XY)Z$ spectra and up to 5 GPa in $\bar{Z}(XX)Z$ spectra. The trends in $\omega(p)$ and $I_n(p)$ that we have detected in the parallel polarized spectra are in full accordance with the Raman analysis on powders by Kreisel *et al.* [50]. The minimum in $\omega(p)$ at 5 GPa along with the constant $I_n(p)$ at pressures above suggest that the reduction of B-cation off-center shifts does not further proceed above 5 GPa. This stabilization of the remaining B-site Ti^{4+} off-centering might be caused by the pressure-induced correlation of the A-site subsystem, indicated by the decrease in the effective $\Gamma(p)$ in both parallel and cross-polarized spectra [Figs. 3(b) and 3(c)]. In contrast to the observations made in NBT-0.048BT, pressure in pure NBT also increases the order within the B-site subsystem, as deduced from the decrease in FWHM [see Figs. 6(b) and 6(c)]. This indicates that the presence of Ba at the A site in the NBT structure hinders any possible ordering in the B-cation subsystem. Additionally, the presence of a $\omega(p)$ minimum at 5 GPa for NBT in contrast to merely a subtle kink in $\omega_{310}(p)$ at ~ 4.5 GPa in NBT-0.048BT demonstrates that Ba doping hinders not only the structural transformations involving the A-site cations but also those concerning the B-site cations. Furthermore, at pressures above 2.7 GPa, where ω_{310} in the Ba-doped compound can be unambiguously ascribed to B-cation off-centering vibrations, the total fractional intensity $I_{n(XX+XY)}$ is larger for NBT-0.048BT than for pure NBT [Fig. 4(b)], indicating that Ba doping prevents the pressure-induced suppression of polar B-cation displacements, like Pb-based relaxors [81].

(d) BO_6 tilting. The tilting vibrations of BO_6 octahedra (between 320 and 420 cm^{-1}) involve also A-O bond stretching within the pseudocubic $\langle 111\rangle$ planes [75,76]. At ambient pressure, NBT-0.048BT does not exhibit any BO_6 tilting detectable by Raman spectroscopy (Fig. 1), which is consistent with the Ba-induced suppression of tilts deduced from neutron total scattering [23]. This is most probably related to the disturbance in coherent off-centered shifts of A-site cations in the presence of Ba, which in turn hinders tilt development. Only above 2.7 GPa can a new peak be identified at $\sim$326 cm^{-1} [Fig. 7(a)]. At 4 GPa, a second minor peak at $\sim$412 cm^{-1} is resolved, followed by a kink in $\omega_{326}(p)$ at $\sim$4.5 GPa. Although the spectral range and the increase in intensity with increasing pressure of the peak at $\sim$326 cm^{-1} indicate that it originates from BO_6 tilting vibrations, it might also be influenced by B-cation off-centering vibrations since, at the same pressure at which it appears, the wave number of the B-localized mode $\omega_{310}(p)$ drops abruptly, and both $\omega_{310}(p)$ and $\omega_{326}(p)$ exhibit a kink at $\sim$4.5 GPa. The appearance and pressure dependence of $\omega_{326}(p)$ and $\omega_{412}(p)$ reveal the occurrence of evolving octahedral tilt pattern between 2.7 and 4.5 GPa, alongside the antipolar order in the A-cation subsystem, which occurs already at $\sim$1.9 GPa. The presence of two Raman signals suggests the existence of octahedral tilts with unequal magnitudes, independently of whether these are antiphase or in-phase tilts [43]. Previous density functional simulations on Pb-based perovskite-type relaxors have revealed that antiphase $a^- a^- c^-$ $(c < a)$ and mixed $a^-a^-c^+$ tilt patterns are thermodynamically preferred at high pressures [43]. Neutron and XRD experiments on Pb-based relaxors have confirmed that, if no tilting is observed at ambient conditions, pressure first induces antiphase $a^- a^- a^-$ order, which upon further pressure increase transforms into $a^- a^- c^-$ $(c < a)$ or mixed $a^-a^-c^+$ [41,43]. On the other hand, TEM at ambient conditions suggests a copresence of local antiphase $a^- a^- a^-$ and in-phase $a^0a^0c^+$ tilt order in NBT-x_{MPB}BT [82,83]. As the $a^0a^0c^+$ tilt order is the thermodynamically most unstable tilt pattern in perovskite oxides at high pressures [43], we can speculate that the appearance of new Raman peaks for $x = 0.048$ indicates the development of an $a^- a^- a^-$ pattern at 2.7 GPa (a single peak at 326 cm^{-1}), which transforms into a mixed $a^-a^-c^+$ tilt pattern at 4.0 GPa (a second Raman peak at 412 cm^{-1}).

For pure NBT at ambient pressure, there are two weak Raman peaks generated by BO_6 tilting at $\sim$375 and $\sim$409 cm^{-1} (Fig. 1, inset). It is worth noting that, for pure NBT, a nanoscale $a^-a^-c^+$ BO_6 tilting pattern was suggested but with a coherence length of the in-phase tilt component significantly shorter than that of the antiphase tilting, resulting in an average tilt pattern $a^- a^- c^-$ typical of Cc [8,84]. The lower-energy peak (at $\sim$375 cm^{-1}) strongly softens up to 1.6 and 2.2 GPa in $\bar{Z}(XX)Z$ and $\bar{Z}(XY)Z$ spectra, respectively, and keeps softening above these charactering pressures but with a considerably lower rate [Figs. 7(b) and 7(c)]. Likewise, the $d\omega(p)/dp$ of the higher-energy peak (at $\sim$409 cm^{-1}) of NBT slightly changes at the abovementioned characteristic pressures. This indicates significant changes in the octahedral tilt pattern at 1.6 and 2.2 GPa, which most probably is due to a pressure-induced transformation of the dominant antiphase tilt pattern into a mixed tilt pattern [49], to facilitate the rearrangements of the off-centered A-site cations, as deduced from the Raman scattering near 50 cm^{-1} (Fig. 3) and synchrotron XRD [19]. The alterations in $\omega(p)$ are accompanied by maxima in the FWHM and fractional intensity of the tilt modes. The $\Gamma(p)$ and $I_{n(377)}(p)$ trends were fitted with Gaussian functions using polynomial functions as baselines. In both parallel and cross-polarized spectra, $\Gamma(p)$ and $I_n(p)$ for the lower-energy peak show a well-pronounced maximum at a pressure where $d\omega(p)/dp$ considerably changes and a second very broad maximum at $\sim$5.0 GPa. The latter pressure is in excellent agreement with that at which the off-center shift of the B-site cations stops reducing (see Fig. 6). The $I_{n(409)}(p)$ trend as well as the gradually increasing baseline of $I_{n(375)}(p)$ indicate that pressure enhances the BO_6 tilting in NBT, like Pb-based relaxors [43,73,76,78,81], while the corresponding $\Gamma(p)$ trends suggest increasing disorder in the tilting patterns. The latter may be related to the ongoing development of unequal tilts around the cubic [100], [010], and [001] directions, which has been detected for Pb-based relaxors via resolved splitting of the corresponding Raman peak [41,43]. Kreisel *et al.* [50] report the occurrence of four new Raman peaks in the range 250–420 cm^{-1} at 5 GPa in NBT powders. Two of those peaks correspond to the peaks near 375 and 409 cm^{-1}, which are already included in our starting model at ambient pressure. Although the goodness of fit did not require the use of additional peaks, we tried to include two more peaks at $\sim$260 and $\sim$395 cm^{-1}, above 5 GPa. The uncertainties in the integrated intensity, however, indicate only an extra peak at $\sim$395 cm^{-1}

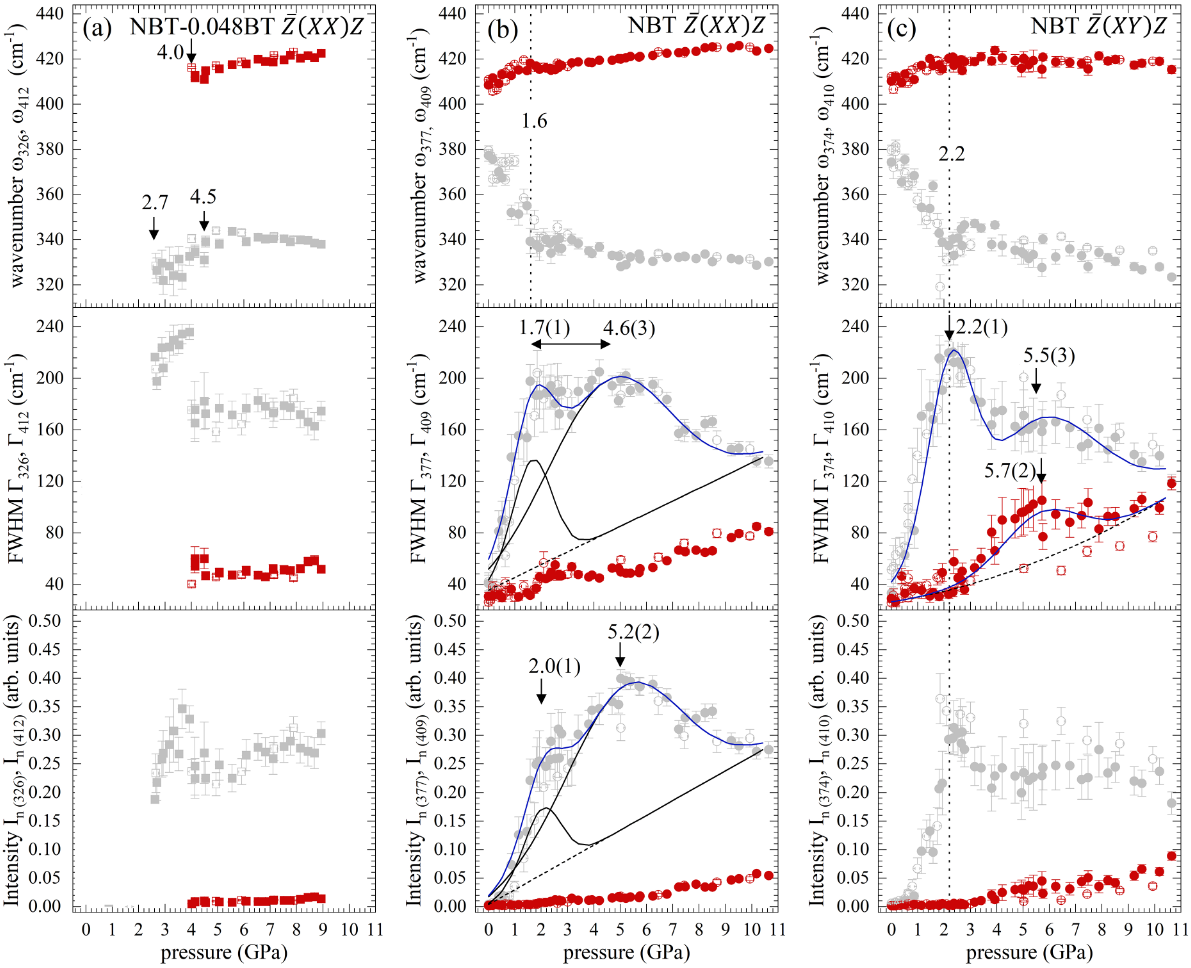

FIG. 7. Pressure dependence of the Raman peak positions (ω), full widths at half maxima (FWHMs; Γ), and fractional intensities (I_n) of the octahedral tilting modes in parallel polarized spectra of (a) NBT-0.048BT and (b) NBT as well as (c) in cross-polarized spectra of NBT. For NBT-0.048BT, the trends in the cross-polarized spectra are the same as in the parallel polarized spectra shown here. Open symbols correspond to data measured on decompression. The solid lines in the $\Gamma(p)$ and $I_n(p)$ plots in (b) and (c) are Gaussian fits to the data points with polynomial baselines (dashed lines). For the sake of limited space, the baseline and individual Gaussian functions are not displayed for Γ_{374} in the $\bar{Z}(XY)Z$ spectra of NBT. The errors in the individual data points stem from the corresponding spectral fit. The errors in the characteristic pressures are derived from Gaussian or linear fits to the data points.

in the parallel polarized spectra could be acceptable, which has negligible effect on the trends of the other modes and does not provide new information about characteristic pressures (see Fig. S6 in the Supplemental Material [71]).

B. In-house single-crystal XRD

The variation of the two unconstrained unit-cell parameters that were determined with high accuracy in the single-crystal high-pressure XRD measurements (referred to hereafter as a_1 and a_2) is reported in Fig. 8(a). These two lattice parameters are identical up to 4 GPa. At this pressure, the a_1 and a_2 axes start to differ from each other, and the difference is above the 2σ standard deviation at 5.4 GPa. The unit-cell lattice parameters were, therefore, constrained to the cubic symmetry (Table SIV in the Supplemental Material [71]) at all pressures, which is a good approximation for the data points <4 GPa and a fair approximation for the two highest data points for sake of comparison. The variation with pressure of the pseudocubic unit-cell volume of NBT-0.048BT, normalized with respect to the respective value at ambient pressure, is shown in Fig. 8(b). Since above 4 GPa the unconstrained unit-cell lattice parameters start deviating from the cubic symmetry, the P-V data have been fitted using a third-order Birch-Murnaghan equation of state (EOS) only up to 3.3 GPa. The resulting bulk modulus is $K_0 = 83.5 \pm 1.7$ GPa with a pressure derivative $K' = 11.4 \pm 2.0$. However, the weighted χ^2 of the fitting $\chi^2_w = 2.42$, is quite large, indicating that such an EOS may not be representative for the entire dataset [85]. Near 0.9 ± 0.1 GPa, V/V_0 significantly deviates from the EOS in a few points [see insert in Fig. 8(b)], indicating complex compressional behavior. Pressure-induced phase transitions as well as changes in compressional mechanism can be better revealed if the p-V data are recalculated in terms of normalized pressure $F = p/[3f(1+2f)^{5/2}]$ vs Eulerian strain $f = [(V_0/V)^{2/3} - 1]/2$ [85]. Here, $F(f)$ data, when lying either on a horizontal or straight line with a positive slope, indicate the absence of a phase transition and can be appropriately fitted using a second- or a third-order Birch-Murnaghan EOS [85], whereas points in $F(f)$ at which

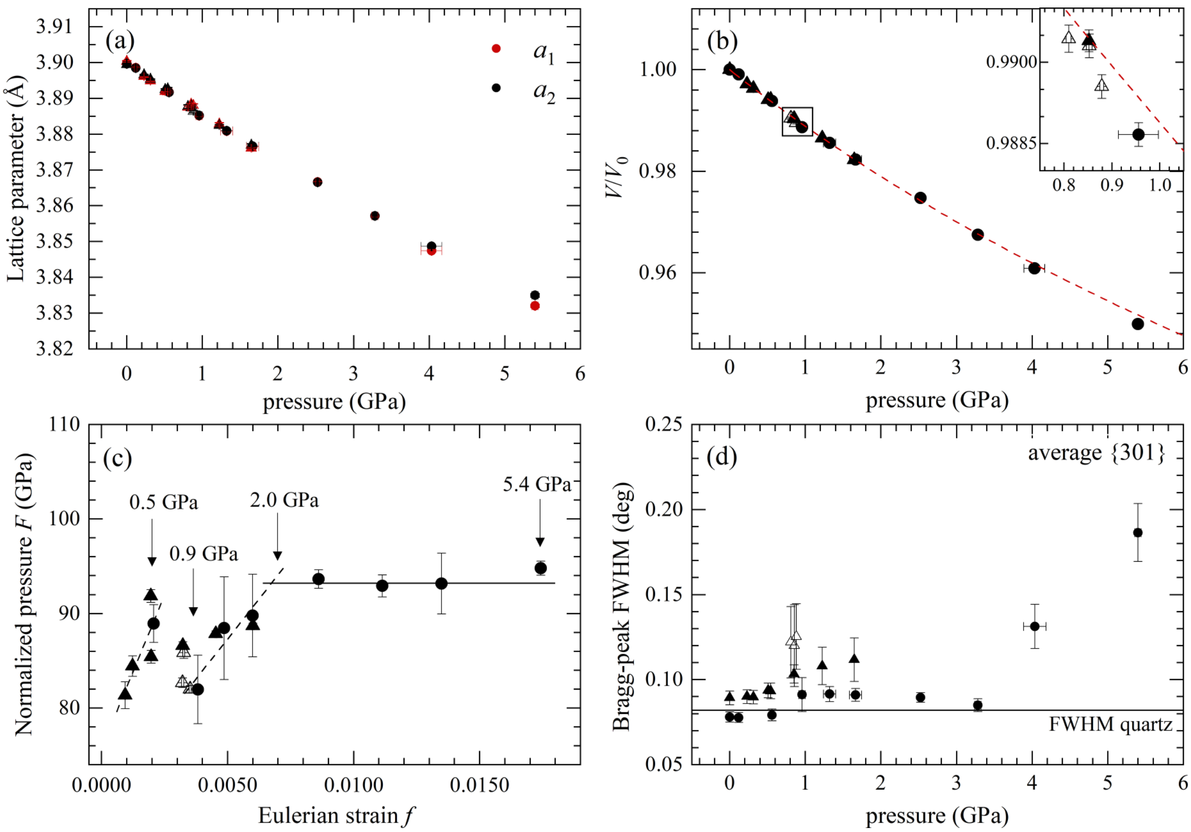

FIG. 8. (a) Pressure dependence of the unconstrained lattice parameters a_1 and a_2; (b) pseudocubic unit-cell volume of NBT-0.048BT normalized to the volume V_0 measured at ambient pressure; (c) the normalized pressure $F = p/[3f(1+2f)^{5/2}]$ plotted against the Eulerian strain $f = [(V_0/V)^{2/3} - 1]/2$ with propagating errors calculated according to Ref. [85]; and (d) pressure evolution of the average full width at half maximum (FWHM) of pseudocubic {301} Bragg reflections as representative for the broadening of the diffraction peaks. Vertical error bars in (a) are smaller than the size of the symbols. The red dashed line in (b) is the third-order Birch-Murnaghan equation of state (EOS) fitted to the data points up to 3.3 GPa. The lines in (c) show the linear fits of the data from 0.23 to 0.56 GPa, from 0.88 to 1.68 GPa (black, dotted), and from 2.5 to 4.0 GPa (black, solid). The horizontal solid line in (d) at 0.082° represents the instrumental resolution via the average FWHM of quartz Bragg reflections. Circles correspond to data points measured in the first pressure run, while triangles to data points measured in the second run. Data points measured on decompression are given by open symbols.

$dF/df = 3K_0(K_0' - 4)f/2 = 0$ are indicative of discontinuity in the bulk modulus, its derivative, or both, which in turn points to a phase transition [43,73,76]. In the pressure range between 0.23 and 1.68 GPa, the $F((f)$ plot of NBT-0.048BT shows three discontinuities at 0.5, 0.9, and ∼2 GPa [Fig. 8(c)]. The maximum at ∼0.5 GPa as well as the minimum at ∼0.9 GPa has been observed for data collected in separate experiments both on compression and decompression and thus likely indicate changes in the elasticity triggered by structural transformations. The feature at ∼0.5 GPa matches the kink in $\omega(p)$ of the lower-energy B-cation mode [see insert in Fig. 6(a)], whereas the feature at ∼0.9 GPa corresponds to the pressure at which this mode disappears (1.0 ± 0.1 GPa). Therefore, the rearrangements in the B-cation subsystem at low pressures, occurring in NBT-0.048BT but not in NBT, appear to also affect the macroscopic elastic strain, likely because of the enhanced elastoelectric response of NBT-xBT at the MPB, although it does not appear to affect the overall pseudocubic symmetry. Above 2 GPa, $F(f)$ remains constant, and the intercept with the F axis of the horizontal lines through the data suggests $K_0 = 93.2$ GPa (with $K' = 4$), indicating a stiffer structure than that at atmospheric pressure. However, the decrease in compressibility with pressure of this high-pressure structure is not as pronounced as that occurring at low pressures (0.23–0.56 and 0.88–1.68 GPa), where the $F(f)$ data lie on very steep straight lines. According to the Raman data, the A- and B-cation subsystems rearrange between ∼1.7 and ∼4.5 GPa. Moreover, at 2.7 ± 0.1 and 4.0 ± 0.1 GPa, there is the appearance of tilt modes [see Fig. 7(a)]. The tilting may, therefore, act as a new compression mechanism allowing the structure to better accommodate at larger pressures, giving rise to a smaller K'. The data point corresponding to 5.4 GPa is slightly above the constant trend in the f-F plot [Fig. 8(b)]. This pressure matches the second maximum (5.6 ± 0.2 GPa) in the $\Gamma_{250}(p)$ of the B-cation mode [see Fig. 6(a)], implying a possible phase transition due to further rearrangements of the B-cation subsystem at ∼5.5 GPa. At this pressure, the violation of the pseudocubic symmetry starts to be significant, as indicated by the unconstrained unit-cell parameters [Fig. 8(a)] as well as by the extensive broadening of the Bragg reflections [Fig. 8(d)]. Such broadening is unlikely to be due to nonhydrostatic stresses, given the small crystal dimensions and the hydrostaticity of the pressure medium used [64]. The broadening, however, hindered the determination of the

TABLE I. Characteristic pressures/pressure ranges (in GPa) of structural transformations for NBT-0.048BT and pure NBT.

NBT-0.048BT		NBT		
Raman	XRD	Raman	XRD/XDS [19]	Structural transformation
0.5–1.0	0.5–0.9			Rearrangements of the *B*-site cations, suppression of the Ba-induced uniaxial local octahedral anisotropy
1.2[a]		∼0.3[a]		Decoupling of adjacent *A*- and *B*-site dipoles
1.9–4.3		1.5–2.2	1.6–2.0	Antipolar order of *A*-cation off-center shifts
		1.6[b]–2.2	1.6–2.0	Change in the BO_6-tilt order pattern
2.7[b]–4.0	2.5–4.0			Development of BO_6 tilt order
4.8		3.7	2.8–3.7	Suppression of the directional dispersion of *A*-cation off-center shifts and increasing of the length of coherence of correlated antiphase *A*-cation shifts
4.5		5.0		Slowdown of the suppression of *B*-cation off-centering; further readjustment in the BO_6 tilt pattern
5.6	5.4			Possible further rearrangement in the *B*-cation subsystem?
			9.9–11.1	Phase transition to a another ferroic phase

[a] Analog of p_1^* in Pb-based relaxor ferroelectrics [40,73].
[b] Analog of p_2^* in Pb-based relaxor ferroelectrics [41,43].

symmetry of the evolving high-pressure phase, which might be orthorhombic *Pnma* or a noncentrosymmetric subgroup of *Pnma*, as it was proposed to develop in pure NBT already above 2 GPa [49]. At 4.0 GPa, a second tilt mode occurs in NBT-0.048BT, followed by a kink at 4.5 GPa of $\omega(p)$ of the primary tilt mode that appeared at 2.7 GPa [see Fig. 7(a)]. Moreover, the evolving antipolar order of off-center shifts of the *A*-site cations is completed at ∼4.5 GPa [Fig. 3(a)]. Therefore, the anomalous broadening of the Bragg peaks may indicate an increase in the ferroic distortion of the atomic structure and a consequent development of ferroic domains, i.e., enhanced mosaicity. Variation in mosaicity should be responsible for the slight difference between the Bragg-peak FWHMs of the two specimens analyzed in the two runs (triangles and circles in Fig. 8) as well as for the subtly incomplete recovery of the Bragg-peak widths on decompression [open symbols in Fig. 8(d)]. However, the broadening of the Bragg peak observed at high pressures recovers on decompression, in full accordance with the Raman data that indicate reversibility of all atomic-scale structural changes induced by pressure.

The bulk modulus of NBT-0.048BT ($K_0 = 83.5 \pm 1.7$ GPa) is smaller than that of pure NBT ($K_0 = 95.2$ GPa [86]). $BaTiO_3$ exhibits a bulk modulus ∼130 GPa [87], which is also considerably larger than that of NBT-0.048BT. Therefore, Ba doping of NBT to the level of MPB significantly softens the material. The bulk modulus of NBT-0.048BT is also smaller than that of Pb-based relaxor ferroelectrics and ferroelectric solid solutions, which typically exhibit a bulk modulus in the range 92–110 GPa [25,81,88,89].

IV. SUMMARY AND CONCLUSIONS

The characteristic pressures of structural transformations in NBT and NBT-0.048BT revealed by Raman scattering and XRD analyses are summarized in Table I.

Like Pb-based relaxor ferroelectrics [40,41,43,73], decoupling of dipoles at adjacent *A* and *B* sites takes place in NBT-*x*BT at a characteristic pressure p_1^* in the range 0.3–1.2 GPa [40,73], and a development or change of existing BO_6 tilt pattern occurs at a higher characteristic pressure p_2^* in the range 1.6–2.7 GPa. Another common feature for both Pb- and Bi-based perovskite-type ferroelectrics is that pressure hinders the off-centering of the *B*-site cations while enhancing antipolar order of *A*-site-cation displacements.

The comparison between NBT and NBT-0.048BT reveals that Ba doping at the level of MBP composition affects the structural response to pressure as follows:

(1) The substitution of Ba^{2+} shifts the rearrangements of the *A*-site cations toward higher pressures, i.e., it hardens the *A*-cation subsystem, most probably via the intrinsic local stresses around Ba^{2+} [25,81] due to its larger ionic radius than Na^+ and Bi^{3+} [90]. By the same reason, it shifts p_1^* to higher pressures.

(2) The *A*-site Ba^{2+} hinders the suppression of the off-centering for both *A*- and *B*-site cations at high pressures.

(3) The *A*-site Ba^{2+} enhances the elastic response of the *B*-site cations and triggers structural alteration that affects the macroscopic strain even before the decoupling of adjacent *A*- and *B*-site dipoles. Moreover, *A*-site Ba^{2+} inhibits the hardening of the *B*-cation subsystem at high pressures, likely driving the reduction of the bulk modulus at the MPB.

(4) The intrinsic chemical pressures associated with the *A*-site Ba^{2+} suppress the BO_6 tilt order at ambient pressure, but these Ba-related local stresses can be overcome by an external high pressure, leading to BO_6 tilt order.

To summarize, although the substitution of larger-sized Ba^{2+} for smaller-sized Na^+ and Bi^{3+} generates local stresses, at the MPB, the incorporation of Ba into the structure softens the material, mainly due to enhanced elastic response of the *B*-cation subsystem.

ACKNOWLEDGMENTS

The authors thank Dr. Alexander Kurnosov, Universität Bayreuth, for help with DAC loading and XRD experiments as well as Dr. Semën Gorfman, Tel Aviv University, for providing the samples. Financial support by the Deutsche Forschungsgemeinschaft (Grants No. MI 1127/12–1 and No. BO 2550/10–1) is gratefully acknowledged.

---

[1] A. S. Bhalla, R. Guo, and R. Roy, The perovskite structure—A review of its role in ceramic science and technology, Mater. Res. Innovations **4**, 3 (2000).

[2] A. M. Glazer, P. A. Thomas, K. Z. Baba-Kishi, G. K. H. Pang, and C. W. Tai, Influence of short-range and long-range order on the evolution of the morphotropic phase boundary in $\mathrm{Pb(Zr_{1-x}Ti_x)O_3}$, Phys. Rev. B **70**, 184123 (2004).

[3] T. Takenaka, H. Nagata, and Y. Hiruma, Phase transition temperatures and piezoelectric properties of $\mathrm{(Bi_{1/2}Na_{1/2})TiO_3}$- and $\mathrm{(Bi_{1/2}K_{1/2})TiO_3}$-based bismuth perovskite lead-free ferroelectric ceramics, IEEE Trans. Ultrason. Ferroelectr. Freq. Control **56**, 1595 (2009).

[4] M. Acosta, N. Novak, V. Rojas, S. Patel, R. Vaish, J. Koruza, G. A. Rossetti, and J. Rödel, $\mathrm{BaTiO_3}$-based piezoelectrics: Fundamentals, current status, and perspectives, Appl. Phys. Rev. **4**, 41305 (2017).

[5] R. Beanland and P. A. Thomas, Imaging planar tetragonal sheets in rhombohedral $\mathrm{Na_{0.5}Bi_{0.5}TiO_3}$ using transmission electron microscopy, Scr. Mater. **65**, 440 (2011).

[6] F. Pforr, M. Major, W. Donner, U. Stuhr, and B. Roessli, Influence of tetragonal platelets on the dielectric permittivity of $\mathrm{0.964Na_{1/2}Bi_{1/2}TiO_3{-}0.036BaTiO_3}$, Phys. Rev. B **94**, 014105 (2016).

[7] D. Maurya, M. Murayama, A. Pramanick, W. T. Reynolds, K. An, and S. Priya, Origin of high piezoelectric response in A-site disordered morphotropic phase boundary composition of lead-free piezoelectric $\mathrm{0.93(Na_{0.5}Bi_{0.5})TiO_3}$-$\mathrm{0.07BaTiO_3}$, J. Appl. Phys. **113**, 114101 (2013).

[8] I. Levin and I. M. Reaney, Nano- and mesoscale structure of $\mathrm{Na_{1/2}Bi_{1/2}TiO_3}$: A TEM perspective, Adv. Funct. Mater. **22**, 3445 (2012).

[9] T. Takenaka, K. Maruyama, and K. Sakata, $\mathrm{(Bi_{0.5}Na_{0.5})TiO_3}$-$\mathrm{BaTiO_3}$ system for lead-free piezoelectric ceramics, Jpn. J. Appl. Phys. **30**, 2236 (1991).

[10] W. Ge, H. Cao, C. Devreugd, J. Li, and D. Viehland, Influence of $\mathrm{BaTiO_3}$ content on the structure and properties of $\mathrm{Na_{0.5}Bi_{0.5}TiO_3}$ crystals, J. Am. Ceram. Soc. **94**, 3084 (2011).

[11] Y. Hiruma, K. Yoshii, H. Nagata, and T. Takenaka, Investigation of phase transition temperatures on $\mathrm{(Bi_{1/2}Na_{1/2})TiO_3}$-$\mathrm{(Bi_{1/2}K_{1/2})TiO_3}$ and $\mathrm{(Bi_{1/2}Na_{1/2})TiO_3}$-$\mathrm{BaTiO_3}$ lead-free piezoelectric ceramics by electrical measurements, Ferroelectrics **346**, 114 (2007).

[12] H. Lidjici, B. Lagoun, M. Berrahal, M. Rguitti, M. A. Hentatti, and H. Khemakhem, XRD, Raman and electrical studies on the $\mathrm{(1\text{-}}x\mathrm{)(Na_{0.5}Bi_{0.5})TiO_3} - x\mathrm{BaTiO_3}$ lead free ceramics, J. Alloys Compd. **618**, 643 (2015).

[13] W. Ge, C. Luo, C. P. Devreugd, Q. Zhang, Y. Ren, J. Li, H. Luo, and D. Viehland, Direct evidence of correlations between relaxor behavior and polar nano-regions in relaxor ferroelectrics: A case study of lead-free piezoelectrics $\mathrm{Na_{0.5}Bi_{0.5}TiO_3}-x\%\mathrm{BaTiO_3}$, Appl. Phys. Lett. **103**, 241914 (2013).

[14] W. Ge, C. P. Devreugd, D. Phelan, Q. Zhang, M. Ahart, J. Li, H. Luo, L. A. Boatner, D. Viehland, and P. M. Gehring, Lead-free and lead-based $AB\mathrm{O_3}$ perovskite relaxors with mixed-valence A-site and B-site disorder: Comparative neutron scattering structural study of $\mathrm{(Na_{1/2}Bi_{1/2})TiO_3}$ and $\mathrm{Pb(Mg_{1/3}Nb_{2/3})O_3}$, Phys. Rev. B **88**, 174115 (2013).

[15] W. Jo, S. Schaab, E. Sapper, L. A. Schmitt, H.-J. Kleebe, A. J. Bell, and J. Rödel, On the phase identity and its thermal evolution of lead free $\mathrm{(Bi_{1/2}Na_{1/2})TiO_3}$-6 mol% $\mathrm{BaTiO_3}$, J. Appl. Phys. **110**, 74106 (2011).

[16] C. Ma, X. Tan, E. Dul'kin, and M. Roth, Domain structure-dielectric property relationship in lead-free $(1{-}x)\mathrm{(Bi_{1/2}Na_{1/2})TiO_{3-}}_x\mathrm{BaTiO_3}$ ceramics, J. Appl. Phys. **108**, 104105 (2010).

[17] G. de La Flor, T. Malcherek, S. Gorfman, and B. Mihailova, Structural transformations in $(1{-}x)\mathrm{Na_{0.5}Bi_{0.5}TiO_3}-x\mathrm{BaTiO_3}$ single crystals studied by Raman spectroscopy, Phys. Rev. B **96**, 214102 (2017).

[18] G. de La Flor and B. Mihailova, Tuning the temperature-induced local-dipole coupling in $(1{-}x)\mathrm{Na_{0.5}Bi_{0.5}TiO_3}-x\mathrm{BaTiO_3}$ via electric field, J. Appl. Phys. **127**, 194103 (2020).

[19] J. Kreisel, P. Bouvier, B. Dkhil, P. A. Thomas, A. M. Glazer, T. R. Welberry, B. Chaabane, and M. Mezouar, High-pressure x-ray scattering of oxides with a nanoscale local structure: Application to $\mathrm{Na_{1/2}Bi_{1/2}TiO_3}$, Phys. Rev. B **68**, 014113 (2003).

[20] M. Gröting, S. Hayn, and K. Albe, Chemical order and local structure of the lead-free relaxor ferroelectric $\mathrm{Na_{1/2}Bi_{1/2}\ TiO_3}$, J. Solid State Chem. **184**, 2041 (2011).

[21] M. Gröting, I. Kornev, B. Dkhil, and K. Albe, Pressure-induced phase transitions and structure of chemically ordered nanoregions in the lead-free relaxor ferroelectric $\mathrm{Na_{1/2}Bi_{1/2}\ TiO_3}$, Phys. Rev. B **86**, 134118 (2012).

[22] Y. Yoneda, H. Nagata, and T. Takenaka, Local structure analysis of $\mathrm{Bi_{0.5}Na_{0.5}TiO_3}$, J. Korean Phys. Soc. **66**, 1339 (2015).

[23] K. Datta, R. B. Neder, A. Richter, M. Göbbels, J. C. Neuefeind, and B. Mihailova, Adaptive strain prompting a pseudo-morphotropic phase boundary in ferroelectric $(1{-}x)\mathrm{Na_{0.5}Bi_{0.5}TiO_3}-x\mathrm{BaTiO_3}$, Phys. Rev. B **97**, 184101 (2018).

[24] G. O. Jones and P. A. Thomas, Investigation of the structure and phase transitions in the novel A-site substituted distorted perovskite compound $\mathrm{Na_{0.5}Bi_{0.5}TiO_3}$, Acta Cryst. B **58**, 168 (2002).

[25] A.-M. Welsch, B. J. Maier, J. M. Engel, B. Mihailova, R. J. Angel, C. Paulmann, M. Gospodinov, A. Friedrich, R. Stosch, B. Güttler *et al.*, Effect of Ba incorporation on pressure-induced structural changes in the relaxor ferroelectric $\mathrm{PbSc_{0.5}Ta_{0.5}O_3}$, Phys. Rev. B **80**, 104118 (2009).

[26] J. Yao, L. Yan, W. Ge, L. Luo, J. Li, D. Viehland, Q. Zhang, and H. Luo, Evolution of domain structures in $\mathrm{Na_{1/2}Bi_{1/2}TiO_3}$ single crystals with $\mathrm{BaTiO_3}$, Phys. Rev. B **83**, 054107 (2011).

[27] J. Yao, N. Monsegue, M. Murayama, W. Leng, W. T. Reynolds, Q. Zhang, H. Luo, J. Li, W. Ge, and D. Viehland, Role of coexisting tetragonal regions in the rhombohedral phase of $\mathrm{Na_{0.5}Bi_{0.5}TiO_3}-x$ at.%$\mathrm{BaTiO_3}$ crystals on enhanced

piezoelectric properties on approaching the morphotropic phase boundary, Appl. Phys. Lett. **100**, 12901 (2012).

[28] B. N. Rao and R. Ranjan, Electric-field-driven monoclinic-to-rhombohedral transformation in $Na_{1/2}Bi_{1/2}TiO_3$, Phys. Rev. B **86**, 134103 (2012).

[29] S. Gorfman and P. A. Thomas, Evidence for a non-rhombohedral average structure in the lead-free piezoelectric material $Na_{0.5}Bi_{0.5}TiO_3$, J. Appl. Cryst. **43**, 1409 (2010).

[30] A. M. Glazer, The classification of tilted octahedra in perovskites, Acta Cryst. B **28**, 3384 (1972).

[31] C. Ma, H. Guo, and X. Tan, A new phase boundary in $(Bi_{1/2}Na_{1/2})TiO_3$-$BaTiO_3$ revealed via a novel method of electron diffraction analysis, Adv. Funct. Mater. **23**, 5261 (2013).

[32] Q. Zhang, X. Zhao, R. Sun, and H. Luo, Crystal growth and electric properties of lead-free NBT-BT at compositions near the morphotropic phase boundary, Phys. Status Solidi A **208**, 1012 (2011).

[33] S.-J. L. Kang, J.-H. Park, S.-Y. Ko, and H.-Y. Lee, Solid-state conversion of single crystals: The principle and the state-of-the-art, J. Am. Ceram. Soc. **98**, 347 (2015).

[34] R. Ranjan and A. Dviwedi, Structure and dielectric properties of $(Na_{0.50}Bi_{0.50})_{1-x}Ba_xTiO_3$: $0 \leqslant x \leqslant 0.10$, Solid State Commun. **135**, 394 (2005).

[35] G. de La Flor, S. Gorfman, and B. Mihailova, Local-scale structural response of $(1–x)Na_{0.5}Bi_{0.5}TiO_3-xBaTiO_3$ to external electric fields, Appl. Phys. Lett. **114**, 42901 (2019).

[36] H. Zhang, G. Deng, A. J. Studer, X. Li, X. Zhao, and H. Luo, Neutron diffuse scattering of $(1–x)(Na_{0.5}Bi_{0.5})TiO_3-xBaTiO_3$ relaxor ferroelectric single crystals, Scr. Mater. **86**, 5 (2014).

[37] S. Zhang, R. Xia, and T. R. Shrout, Lead-free piezoelectric ceramics vs. PZT? J. Electroceram. **19**, 251 (2007).

[38] B. Mihailova, M. Gospodinov, B. Güttler, R. Stosch, and U. Bismayer, Ferroic clustering and phonon anomalies in Pb-based perovskite-type relaxors, J. Phys.: Condens. Matter **19**, 275205 (2007).

[39] P. Fan, K. Liu, W. Ma, H. Tan, Q. Zhang, L. Zhang, C. Zhou, D. Salamon, S.-T. Zhang, Y. Zhang *et al.*, Progress and perspective of high strain NBT-based lead-free piezoceramics and multilayer actuators, J. Materiomics **7**, 508 (2021).

[40] B. Mihailova, R. J. Angel, B. J. Maier, A.-M. Welsch, J. Zhao, M. Gospodinov, and U. Bismayer, The structural state of lead-based relaxor ferroelectrics under pressure, IEEE Trans. Ultrason. Ferroelectr. Freq. Control **58**, 1905 (2011).

[41] B. Mihailova, N. Waeselmann, B. J. Maier, R. J. Angel, T. Prüßmann, C. Paulmann, M. Gospodinov, and U. Bismayer, Chemically induced renormalization phenomena in Pb-based relaxor ferroelectrics under high pressure, J. Phys.: Condens. Matter **25**, 115403 (2013).

[42] N. Waeselmann, B. Mihailova, M. Gospodinov, and U. Bismayer, *In situ* high-temperature high-pressure Raman spectroscopy on single-crystal relaxor ferroelectrics $PbSc_{1/2}Ta_{1/2}O_3$ and $PbSc_{1/2}Nb_{1/2}O_3$, J. Phys.: Condens. Matter **25**, 155902 (2013).

[43] B. J. Maier, N. Waeselmann, B. Mihailova, R. J. Angel, C. Ederer, C. Paulmann, M. Gospodinov, A. Friedrich, and U. Bismayer, Structural state of relaxor ferroelectrics $PbSc_{0.5}Ta_{0.5}O_3$ and $PbSc_{0.5}Nb_{0.5}O_3$ at high pressures up to 30 GPa, Phys. Rev. B **84**, 174104 (2011).

[44] B. Mihailova, B. J. Maier, T. Steilmann, E. Dul'kin, and M. Roth, Electric-field-induced local structural phenomena in Pb-based ABO_3-type relaxor ferroelectrics, IEEE Trans. Ultrason. Ferroelectr. Freq. Control **62**, 7 (2015).

[45] B. Mihailova, N. Waeselmann, B. J. Maier, A.-M. Welsch, R. J. Angel, and U. Bismayer, Pressure-induced structural transformations in advanced ferroelectrics with relaxor behaviour, High Pressure Res. **33**, 595 (2013).

[46] N. Waeselmann, B. J. Maier, B. Mihailova, R. J. Angel, J. Zhao, M. Gospodinov, C. Paulmann, N. Ross, and U. Bismayer, Pressure-induced structural transformations in pure and Ru-doped $0.9PbZn_{1/3}Nb_{2/3}O_3$-$0.1PbTiO_3$ near the morphotropic phase boundary, Phys. Rev. B **85**, 014106 (2012).

[47] P. B. Groszewicz, M. Gröting, H. Breitzke, W. Jo, K. Albe, G. Buntkowsky, and J. Rödel, Reconciling local structure disorder and the relaxor state in $(Bi_{1/2}Na_{1/2})TiO_3$-$BaTiO_3$, Sci. Rep. **6**, 31739 (2016).

[48] G. O. Jones, Investigation of the Structure and Phase Transitions in the Novel A-site Substituted Perovskite Series $(Na_{1-x}K_x)_{0.5}Bi_{0.5}TiO_3$, PhD Thesis, (University of Warwick, 2001).

[49] P. A. Thomas, J. Kreisel, A. M. Glazer, P. Bouvier, Q. Jiang, and R. Smith, The high-pressure structural phase transitions of sodium bismuth titanate, Z. Krist. Cryst. Mater. **220**, 717 (2005).

[50] J. Kreisel, A. M. Glazer, P. Bouvier, and G. Lucazeau, High-pressure Raman study of a relaxor ferroelectric: The $Na_{0.5}Bi_{0.5}TiO_3$ perovskite, Phys. Rev. B **63**, 174106 (2001).

[51] C. Xu, D. He, H. Wang, C. Liu, S. Yin, K. Wang, J. Guan, F. Peng, and Z. Kou, High pressure *in situ* differential thermal analysis of $Na_{0.5}Bi_{0.5}TiO_3$ phase transitions up to 5 GPa, J. Alloys Compd. **533**, 9 (2012).

[52] S. Trujillo, J. Kreisel, Q. Jiang, J. H. Smith, P. A. Thomas, P. Bouvier, and F. Weiss, The high-pressure behaviour of Ba-doped $Na_{1/2}Bi_{1/2}TiO_3$ investigated by Raman spectroscopy, J. Phys.: Condens. Matter **17**, 6587 (2005).

[53] Q. Zheng, Q. Li, S. Xue, Y. Wu, L. Wang, Q. Zhang, X. Qin, X. Zhao, F. Wang, and W. Yang, Pressure driven structural evolutions of $0.935(Na_{0.5}Bi_{0.5})TiO_3$-$0.065BaTiO_3$ lead-free ferroelectric single crystal through Raman spectroscopy, Chin. Phys. Lett. **38**, 26102 (2021).

[54] D. Schütz, M. Deluca, W. Krauss, A. Feteira, T. Jackson, and K. Reichmann, Lone-pair-induced covalency as the cause of temperature- and field-induced instabilities in bismuth sodium titanate, Adv. Funct. Mater. **22**, 2285 (2012).

[55] S. Klotz, J.-C. Chervin, P. Munsch, and G. Le Marchand, Hydrostatic limits of 11 pressure transmitting media, J. Phys. D. **42**, 75413 (2009).

[56] K. Takemura, Hydrostaticity in high pressure experiments: Some general observations and guidelines for high pressure experimenters, High Pressure Res. **41**, 155 (2021).

[57] M. Woll, M. Burianek, D. Klimm, S. Gorfman, and M. Mühlberg, Characterization of $(Bi_{0.5}Na_{0.5})_{1-x}Ba_x\ TiO_3$ grown by the TSSG method, J. Cryst. Growth **401**, 351 (2014).

[58] R. Boehler and K. de Hantsetters, New anvil designs in diamond-cells, High Pressure Res. **24**, 391 (2004).

[59] G. Shen, Y. Wang, A. Dewaele, C. Wu, D. E. Fratanduono, J. Eggert, S. Klotz, K. F. Dziubek, P. Loubeyre, O. V. Fat'yanov *et al.*, Toward an international practical pressure scale: A proposal for an IPPS ruby gauge (IPPS-Ruby2020), High Pressure Res. **40**, 299 (2020).

[60] H. Kuzmany, *Solid-State Spectroscopy* (Springer, Berlin, Heidelberg, 2009).

[61] B. Mihailova, N. Waeselmann, C. Stangarone, R. J. Angel, M. Prencipe, and M. Alvaro, The pressure-induced phase transition(s) of $ZrSiO_4$: Revised, Phys. Chem. Miner. **46**, 807 (2019).

[62] OriginPro, Version 2021. OriginLab Corporation, Northampton, MA, USA.

[63] I. Kantor, V. Prakapenka, A. Kantor, P. Dera, A. Kurnosov, S. Sinogeikin, N. Dubrovinskaia, and L. Dubrovinsky, BX90: A new diamond anvil cell design for x-ray diffraction and optical measurements, Rev. Sci. Instrum. **83**, 125102 (2012).

[64] R. J. Angel, M. Bujak, J. Zhao, G. D. Gatta, and S. D. Jacobsen, Effective hydrostatic limits of pressure media for high-pressure crystallographic studies, J. Appl. Cryst. **40**, 26 (2007).

[65] K. S. Scheidl, A. Kurnosov, D. M. Trots, T. Boffa Ballaran, R. J. Angel, and R. Miletich, Extending the single-crystal quartz pressure gauge up to hydrostatic pressure of 19 GPa, J. Appl. Cryst. **49**, 2129 (2016).

[66] D. M. Trots, A. Kurnosov, L. Vasylechko, M. Berkowski, T. Boffa Ballaran, and D. J. Frost, Elasticity and equation of state of $Li_2B_4O_7$, Phys. Chem. Miner. **38**, 561 (2011).

[67] R. J. Angel and L. W. Finger, SINGLE: A program to control single-crystal diffractometers, J. Appl. Cryst. **44**, 247 (2011).

[68] R. L. Ralph and L. W. Finger, A computer program for refinement of crystal orientation matrix and lattice constants from diffractometer data with lattice symmetry constraints, J. Appl. Cryst. **15**, 537 (1982).

[69] H. E. King and L. W. Finger, Diffracted beam crystal centering and its application to high-pressure crystallography, J. Appl. Cryst. **12**, 374 (1979).

[70] K. Datta, A. Richter, M. Göbbels, R. B. Neder, and B. Mihailova, Atomistic origin of huge response functions at the morphotropic phase boundary of $(1–x)Na_{0.5}Bi_{0.5}TiO_3-x$ $BaTiO_3$, Phys. Rev. B **90**, 064112 (2014).

[71] See Supplemental Material at http://link.aps.org/supplemental/10.1103/PhysRevB.108.094110 for additional figures and tables.

[72] J. Kreisel, A. M. Glazer, G. O. Jones, P. A. Thomas, L. Abello, and G. Lucazeau, An x-ray diffraction and Raman spectroscopy investigation of *A*-site substituted perovskite compounds: The $(Na_{1-x}K_x)_{0.5}Bi_{0.5}TiO_3$ $(0 \leqslant x \leqslant 1)$ solid solution, J. Phys.: Condens. Matter **12**, 3267 (2000).

[73] B. Mihailova, R. J. Angel, A.-M. Welsch, J. Zhao, J. Engel, C. Paulmann, M. Gospodinov, H. Ahsbahs, R. Stosch, B. Güttler *et al.*, Pressure-Induced Phase Transition in $PbSc_{0.5}Ta_{0.5}O_3$ as a Model Pb-Based Perovksite-Type Relaxor Ferroelectric, Phys. Rev. Lett. **101**, 017602 (2008).

[74] D. S. Keeble, E. R. Barney, D. A. Keen, M. G. Tucker, J. Kreisel, and P. A. Thomas, Bifurcated polarization rotation in bismuth-based piezoelectrics, Adv. Funct. Mater. **23**, 185 (2013).

[75] B. Mihailova, U. Bismayer, B. Güttler, M. Gospodinov, and L. Konstantinov, Local structure and dynamics in relaxor-ferroelectric $PbSc_{1/2}Nb_{1/2}O_3$ and $PbSc_{1/2}Ta_{1/2}O_3$ single crystals, J. Phys.: Condens. Matter **14**, 1091 (2002).

[76] A.-M. Welsch, B. J. Maier, B. Mihailova, R. J. Angel, J. Zhao, C. Paulmann, J. M. Engel, M. Gospodinov, V. Marinova, and U. Bismayer, Transformation processes in relaxor ferroelectric $PbSc_{0.5}Ta_{0.5}O_3$ heavily doped with Nb and Sn, Z. Krist. **226**, 126 (2011).

[77] K. Datta, A. Richter, M. Göbbels, R. B. Neder, and B. Mihailova, Mesoscopic-scale structrue and dynamics near the morphotropic phase boundary of $(1–x)PbTiO_3-xBiScO_3$, Phys. Rev. B **92**, 024107 (2015).

[78] A.-M. Welsch, B. Mihailova, M. Gospodinov, R. Stosch, B. Güttler, and U. Bismayer, High pressure Raman spectroscopic study on the relaxor ferroelectric $PbSc_{0.5}Nb_{0.5}O_3$, J. Phys.: Condens. Matter **21**, 235901 (2009).

[79] U. Bismayer, Hard mode Raman spectroscopy and its application to ferroelastic and ferroelectric phase transitions, Phase Transitions **27**, 211 (1990).

[80] F. A. Pina Binvignat, T. Malcherek, R. J. Angel, C. Paulmann, J. Schlüter, and B. Mihailova, Radiation-damaged zircon under high pressures, Phys. Chem. Miner. **45**, 981 (2018).

[81] B. J. Maier, A.-M. Welsch, R. J. Angel, B. Mihailova, J. Zhao, J. M. Engel, L. A. Schmitt, C. Paulmann, M. Gospodinov, A. Friedrich *et al.*, A-site doping-induced renormalization of structural transformations in the $PbSc_{0.5}Nb_{0.5}O_3$ relaxor ferroelectric under high pressure, Phys. Rev. B **81**, 174116 (2010).

[82] A. Neagu and C.-W. Tai, Investigation of local structural phase transitions in $95Na_{0.5}Bi_{0.5}TiO_3-5BaTiO_3$ piezoceramics by means of *in-situ* transmission electron microscopy, J. Appl. Phys. **123**, 244105 (2018).

[83] A.-K. Fetzer, A. Wohninsland, K. V. Lalitha, and H.-J. Kleebe, Nanoscale polar regions embedded within ferroelectric domains in $Na_{1/2}Bi_{1/2}TiO_3$-$BaTiO_3$, Phys. Rev. Mater. **6**, 64409 (2022).

[84] H. T. Stokes, E. H. Kisi, D. M. Hatch, and C. J. Howard, Group-theoretical analysis of octahedral tilting in ferroelectric perovskites, Acta Cryst. B **58**, 934 (2002).

[85] R. J. Angel, Equations of state, Rev. Mineral. Geochem. **41**, 35 (2000).

[86] J. Suchanicz, Elastic constants of $Na_{0.5}Bi_{0.5}TiO_3$ single crystal, J. Mater. Sci. **37**, 489 (2002).

[87] H.-Y. Zhang, Z.-Y. Zeng, Y.-Q. Zhao, Q. Lu, and Y. Cheng, First-principles study of lattice dynamics, structural phase transition, and thermodynamic properties of barium titanate, Z. Naturforsch. **71**, 759 (2016).

[88] M. Ahart, R. E. Cohen, V. Struzhkin, E. Gregoryanz, D. Rytz, S. A. Prosandeev, H. Mao, and R. J. Hemley, High-pressure Raman scattering and x-ray diffraction of the relaxor ferroelectric $0.96Pb(Zn_{1/3}Nb_{2/3})O_3$-$0.04PbTiO_3$, Phys. Rev. B **71**, 144102 (2005).

[89] G. Fraysse, A. Al-Zein, J. Haines, J. Rouquette, V. Bornand, P. Papet, C. Bogicevic, and S. Hull, Competing order parameters in the $Pb(Zr_{1-x}Ti_x)O_3$ solid solution at high pressure, Phys. Rev. B **84**, 144110 (2011).

[90] R. D. Shannon, Revised effective ionic radii and systematic studies of interatomic distances in halides and chalcogenides, Acta Cryst. A **32**, 751 (1976).